

Photometric Redshifts for the Hyper Suprime-Cam Subaru Strategic Program Data Release 1

Masayuki Tanaka¹, Jean Coupon², Bau-Ching Hsieh³, Sogo Mineo¹,
Atsushi J. Nishizawa⁴, Joshua Speagle⁵, Hisanori Furusawa¹, Satoshi
Miyazaki^{1,6}, Hitoshi Murayama^{7,8,9}

¹National Astronomical Observatory of Japan, 2-21-1 Osawa, Mitaka, Tokyo 181-8588, Japan

²Department of Astronomy, University of Geneva, ch. d'Écogia 16, 1290 Versoix, Switzerland

³Academia Sinica Institute of Astronomy and Astrophysics, P.O. Box 23-141, Taipei 10617, Taiwan

⁴Institute for Advanced Research, Nagoya University Furocho, Chikusa-ku, Nagoya, 464-8602 Japan

⁵Harvard University, 60 Garden St., Cambridge, MA 02138, USA

⁶SOKENDAI(The Graduate University for Advanced Studies), Mitaka, Tokyo, 181-8588, Japan

⁷Kavli Institute for the Physics and Mathematics of the Universe (Kavli IPMU, WPI), University of Tokyo, Chiba 277-8582, Japan

⁸Department of Physics and Center for Japanese Studies, University of California, Berkeley, CA 94720, USA

⁹Theoretical Physics Group, Lawrence Berkeley National Laboratory, MS 50A-5104, Berkeley, CA 94720

*E-mail: masayuki.tanaka@nao.ac.jp

Received ; Accepted

Abstract

Photometric redshifts are a key component of many science objectives in the Hyper Suprime-Cam Subaru Strategic Program (HSC-SSP). In this paper, we describe and compare the codes used to compute photometric redshifts for HSC-SSP, how we calibrate them, and the typical accuracy we achieve with the HSC five-band photometry (*grizy*). We introduce a new point estimator based on an improved loss function and demonstrate that it works better than other commonly used estimators. We find that our photo- z 's are most accurate at $0.2 \lesssim z_{\text{phot}} \lesssim 1.5$, where we can straddle the 4000Å break. We achieve $\sigma(\Delta z_{\text{phot}}/(1+z_{\text{phot}})) \sim 0.05$ and an outlier rate of about 15% for galaxies down to $i = 25$ within this redshift range. If we limit to a brighter sample of $i < 24$, we achieve $\sigma \sim 0.04$ and $\sim 8\%$ outliers. Our photo- z 's should thus enable many science cases for HSC-SSP. We also characterize the accuracy of our redshift probability distribution function (PDF) and discover that some codes over/under-estimate the redshift uncertainties, which have implications for $N(z)$ reconstruction. Our photo- z products for the entire area in the Public Data Release 1 are publicly available, and both our catalog products (such as point estimates) and full PDFs can be retrieved from the data release site, <https://hsc-release.mtk.nao.ac.jp/>.

Key words: surveys, galaxies: distances and redshifts, galaxies: general, cosmology: observations

1 Introduction

In the era of wide and deep imaging surveys, the photometric redshift technique (hereafter photo- z , see Hildebrandt et al. 2010 and references therein) has become compulsory to uncover the large-scale distance and time information of millions (soon billions) of galaxies. While photo- z algorithms and the photometry measurements have improved significantly over the past two decades (Coupon et al. 2009; Hildebrandt et al. 2008; Hildebrandt et al. 2012; Dahlen et al. 2013; Bonnett et al. 2016), the challenge of acquiring photo- z estimates accurate enough to meet the requirements of cosmology and galaxy evolution studies continues to motivate the active development of photometry extraction and photo- z algorithms even today.

It is now clear that both template-fitting and machine-learning methods are complementary and necessary to compute meaningful photo- z 's. Template-fitting methods (Arnouts et al. 1999; Bolzonella et al. 2000; Feldmann et al. 2006; Brammer et al. 2008; Kotulla et al. 2009) use known galaxy spectral energy distributions (SED) and priors (Benitez 2000; Ilbert et al. 2006; Tanaka 2015) to match the observed colors with predicted ones. Such an approach currently represents the only way to provide photo- z estimates in regions of color/magnitude space where no reference redshifts are available (but see also Leistedt & Hogg 2016). Machine learning methods (Tagliaferri et al. 2003; Collister & Lahav 2004; Lima et al. 2008; Wolf et al. 2009; Carliles et al. 2010; Singal et al. 2011; Brescia et al. 2016) are complementary as they provide efficient photo- z estimates, in terms of speed and precision, but require a training sample that is a fair representation of the galaxy sample of interest, which is often difficult to construct due to missing regions in the multi-color space.

Precise photo- z 's are needed to enable the selection of sharp, non-overlapping redshift bins to “slice” the Universe. For example, cosmic shear studies (Kilbinger et al. 2013; Hildebrandt et al. 2017) suffer from galaxies in adjacent redshift bins that dilute the cosmological signal and increase the importance of systematic biases such as the galaxy intrinsic alignments (Heymans et al. 2013). For galaxy evolution studies, it is often important to infer physical properties of galaxies such as stellar mass in addition to redshifts. It is thus crucial to minimize catastrophic photo- z errors that lead to erroneous physical parameters.

The accurate characterization of the true underlying redshift distribution of a galaxy sample remains a major challenge in today's experiments. With samples composed of hundreds of millions of galaxies, systematic biases now largely dominate over statistical errors, and gathering a complete and numerous cali-

bration sample has become increasingly pressing in the context of current and planned large-scale imaging surveys. Recently, significant progress has been made in building fainter spectroscopic redshift (hereafter spec- z) samples, e.g., DEEP2 (Davis et al. 2003; Cooper et al. 2011; Cooper et al. 2012; Newman et al. 2013), VVDS (Le Fèvre et al. 2004; Le Fèvre et al. 2005; Le Fèvre et al. 2013), VUDS (Tasca et al. 2016), and 3D-HST (Skelton et al. 2014; Momcheva et al. 2016). These are complemented by larger but shallower surveys such as VIPERS (Garilli et al. 2014), SDSS (Alam et al. 2015), Wiggle-Z (Drinkwater et al. 2010) and GAMA (Liske et al. 2015). More complete but with lower redshift resolution samples are also available from PRIMUS (Coil et al. 2011; Cool et al. 2013) along with many-band photo- z 's from COSMOS (Laigle et al. 2016). In parallel, the community has developed new powerful tools to identify deficiencies in existing spec- z samples (see e.g. Masters et al. 2015) in order to help focus resources on targeting specific galaxy populations with the adequate instruments.

Still, additional effort is required to (1) improve photo- z algorithms to fully exploit the information provided by the calibration samples, (2) gather and homogenize heterogeneous datasets, and (3) fill in the underrepresented regions of color/magnitude space with reference redshifts in order to calibrate all of the galaxies observed in the deepest photometric surveys.

These challenges are faced by all on-going and future large-scale photometric surveys, such as the Kilo-Degree Survey (KiDS, de Jong et al. 2013) which started in 2011 and whose aim is to map 1500 deg² in four optical filters (u, g, r, i) at relatively shallow depths. At a similar depth but over a larger area, the Dark Energy Survey (DES, Flaugher 2005) is surveying 5000 deg² in five filters (g, r, i, z, Y) in the southern sky since 2013. In the future, Euclid (Laureijs et al. 2011), a space mission to be launched in 2020, will observe 15000 deg² in one optical (“vis”) and three near-infrared (Y, J, H) filters, complemented by optical multi-wavelength imaging data from the ground. The Large Synoptic Survey Telescope (LSST, Ivezić et al. 2008) will cover 20000 deg² square degrees in 6 filters (u, g, r, i, z, y) over a period of 10 years, starting from 2022, with significantly deeper imaging data than the projects described above.

Here we present the photo- z results from the Hyper-Suprime-Cam Subaru Strategic Program (HSC-SSP, Aihara et al. 2017; Aihara et al. 2017b), a 300-night deep imaging survey dedicated to cosmology and the study of galaxy formation and evolution. The survey consists of three components: a Wide

layer ($r \sim 26$ at 5σ for point sources) over 1400 deg^2 , a Deep layer ($r \sim 27$) over 28 deg^2 , and an UltraDeep layer ($r \sim 28$) over 4 deg^2 . This paper presents the efforts led by the photo- z team in HSC-SSP to develop new photo- z algorithms, gather a state-of-the-art reference redshift sample, deal with an unprecedented amount of data, and release our products to the public.

The data presented in this study correspond to the Public Data Release 1 (PDR1) and the S16A internal data release. In Section 2, we describe the procedures used to build a robust training sample and to validate our photo- z estimates. In Section 3, we present our photo- z methods. Section 4 defines our adopted performance metrics. In Sections 5 and 6, we characterize our photo- z performance. We give an overview of our photo- z products included in the public release in Section 7 and finally conclude in Section 8. As our previous internal photo- z releases are often used in our science papers, we briefly summarize our previous data products in Appendix 1. Unless otherwise stated, all the magnitudes are AB magnitudes.

2 Training, Validation, and Test Samples

The HSC-SSP survey footprint has been designed in order to maximize the overlap with other photometric and spectroscopic surveys, while keeping the survey geometry simple. For photo- z purposes, this means we can exploit a large number of public spectroscopic redshifts in our survey fields and use them to calibrate our photo- z 's. This section describes how we construct the training sample, and how we calibrate, validate and test our photo- z codes (details of the codes can be found in Section 3).

2.1 Construction of the training sample

We first collect spectroscopic redshifts from the literature: zCOSMOS DR3 (Lilly et al. 2009), UDSz (Bradshaw et al. 2013; McLure et al. 2013), 3D-HST (Skelton et al. 2014; Momcheva et al. 2016), FMOS-COSMOS (Silverman et al. 2015), VVDS (Le Fèvre et al. 2013), VIPERS PDR1 (Garilli et al. 2014), SDSS DR12 (Alam et al. 2015), GAMA DR2 (Liske et al. 2015), WiggleZ DR1 (Drinkwater et al. 2010), DEEP2 DR4 (Davis et al. 2003; Newman et al. 2013), and PRIMUS DR1 (Coil et al. 2011; Cool et al. 2013). As each of these surveys have its own flagging scheme to indicate redshift confidence, we homogenize them for selection of secure redshift. The redshifts and flags are fed to the HSC database and matched with the HSC objects. This public spec- z table (described in detail on the spec- z page at the data release site) is included in the PDR1 of HSC-SSP and made available to the community.

Our training data include $\sim 170\text{k}$ and 37k high-quality spec- z and g/prism- z , respectively, taken from the matched catalogs described above. We supplement the training data with $\sim 170\text{k}$ COSMOS2015 many-band photo- z s (Laigle et al. 2016) along

with a collection of private COSMOS spec- z s (Mara Salvato, private communication) exclusively used for our photo- z training (they are *not* included in the PDR1). Data are included in our training set if they meet the following quality cuts:

Public spec- z data:

1. $0.01 < z < 9$ (no stars, quasars, or failures)
2. $\sigma_z < 0.005(1+z)$ (error cut)
3. SDSS/BOSS: zWarning = 0 (no apparent issues)
4. DEEP2: qFlag = 4 ($> 99.5\%$ confidence)
5. PRIMUS: qFlag = 4 (very confident)
6. VIPERS: qFlag = 3 – 4 ($> 95\%$ confidence)
7. VVDS: qFlag = 3 – 4 ($> 95\%$ confidence)
8. GAMA: qFlag ≥ 4 (very confident)
9. WiggleZ: qFlag ≥ 4 (very confident)
10. UDSz: qFlag ≥ 4 (provisional catalog only includes $> 95\%$ confidence)
11. FMOS-COSMOS: qFlag = 3 – 4, $z > 0.01$, flag_star is False ($> 95\%$ confidence with no stars).

3DHST data:

1. flag_star is False (no stars)
2. $0 < z < 9$ (no stars, quasars, or redshift failures)
3. $\max(z_{82} - z_{50}, z_{50} - z_{18}) < 0.05(1+z)$ (1σ redshift dispersion $< 5\%$)
4. $\max(z_{97.5} - z_{50}, z_{50} - z_{2.5}) < 0.1(1+z)$ (2σ redshift dispersion $< 10\%$)

COSMOS data:

1. Spec- z :
 - (a) $3 \leq \text{qFlag} < 6$ ($> 99\%$ confidence)
 - (b) $0 < z < 7$ (no stars or quasars)
 - (c) For objects with repeat observations, $\sigma_z < 0.005(1+z)$ (redshifts agree to within 0.5%)
2. Photo- z :
 - (a) flag_capak is False (no bad photometry)
 - (b) type = 0 (only galaxies)
 - (c) $\chi^2(\text{gal}) < \chi^2(\text{star})$ and $\chi^2(\text{gal})/N_{\text{bands}} < 5$ (fits are reasonable and better than stellar alternatives)
 - (d) $z_{\text{secondary}} < 0$ (no secondary peaks)
 - (e) $\log M_* > 7.5$ (stellar mass recovery successful)
 - (f) $0 < z < 9$ (no stars, quasars, nor X-ray detected sources)
 - (g) $\max(z_{84} - z_{50}, z_{50} - z_{16}) < 0.05(1+z)$ (1σ redshift dispersion $< 5\%$)

Objects are subsequently matched directly to a set target UltraDeep/Deep catalogs selected using the following criteria:

1. detect_is_primary is True (no duplicates)
2. [grizy] cmodel_flux_flags is False
3. [grizy] flags_pixel_edge is False
4. [grizy] flags_pixel_interpolated_center is False
5. [grizy] flags_pixel_saturated_center is False
6. [grizy] flags_pixel_cr_center is False
7. [grizy] flags_pixel_bad is False

8. `[grizy]centroid_sdss_flags` is `False`

These are designed to maximize completeness while removing objects with unreliable photometry. Objects are iteratively matched to this modified catalog within 1 arcsec at (1) UltraDeep, (2) Deep, and (3) Wide depths in order to take advantage of higher-S/N data when available while avoiding possible duplicates.

The following quantities are then selected and/or computed:

1. **Identifiers:** ID, (ra, dec), and (tract, patch) coordinates.
2. **Fluxes:** PSF fluxes, `cmodel` fluxes, `cmodel_exp` fluxes, `cmodel_dev` fluxes, and PSF-matched aperture fluxes with target 1.1 arcsec PSF and 1.5 arcsec apertures taken from the afterburner run (afterburner fluxes; Aihara et al. 2017).
3. **Shapes:** `sdss_shape` parameters.
4. **Miscellaneous:** merge measurement flags, attenuation estimates (`a_[grizy]`), and `extendedness` measurements.
5. **Redshift:** redshift, 1σ error, parent survey (SDSS, etc.), and redshift type (spectroscopic, `g/prism`, or many-band photometric).
6. **Depth:** flag for UltraDeep, Deep, and Wide photometry.
7. **Emulated errors:** emulated wide-depth photometric errors. These are relevant for objects from the Deep and UltraDeep layers, which have smaller photometric uncertainties than Wide due to the deeper depths. They are computed independently for each flux type (PSF, `cmodel`, etc.) by assigning signal-to-noise (S/N) values from a *grizy* nearest-neighbor search to a Wide catalog of $\sim 500k$ objects selected to mimic the overall survey sample.
8. **Weights:** Color/magnitude weights are computed using a generalization of Lima et al. (2008)'s nearest neighbor approach. The color-magnitude distribution of the training sample is different from that of target sample from the Wide layer. The weights are computed so that the training sample can reproduce the color-magnitude distribution of the target galaxies. See Speagle et al. (in prep.) for more details.

The underlying and re-weighted magnitude and redshift distributions of our training sample are shown in Figures 1 and 2, respectively.

As described here, our training sample consists of various redshift measurements (spec, `g/prism`, and many-band photo- z 's). We use all of them as the 'truth' throughout the paper, but some of the redshifts (especially the many-band photo- z 's) may be erroneous. We thus urge caution when interpreting the absolute numbers in our adopted metrics. We refer to these 'true' redshifts as reference redshifts (z_{ref}) throughout the paper.

2.2 Training and validation procedures

The training sample is split into $k = 5$ randomized 'folds'. Because each fold has a relatively large number of objects ($\sim 75k$), most of us employ a simple hold-out validation to train

and validate our photo- z methods. To be specific, we use folds $k = 1 - 3$ to train our codes and $k = 4$ to validate them, with the last fold ($k = 5$) reserved for testing (see below). The only exception here is FRANKEN-Z, which uses cross-validation (i.e., it used 5 rotating folds for training and validation). Throughout the paper, all statistics are computed using the color-magnitude weights described in the previous section.

2.3 Test samples

We reserve a test sample from the training sample in order to evaluate the performance of our codes. Most of us use the subsample of the training sample described in the previous section (the 5th fold). For FRANKEN-Z, we use one of the 5-fold cross-validation runs. We use the test sample to evaluate our performance at the UltraDeep depth. This is reasonable because a significant fraction of the objects in the test sample come from UltraDeep COSMOS, especially at faint magnitudes.

For the Wide-depth performance evaluation, we stack a subsample of the COSMOS UltraDeep data to the Wide depth in all the bands. We have computed the emulated Wide-depth photometric uncertainties as described earlier, but they turn out to be problematic in a few cases. Some of our codes use multiple photometry techniques (e.g., EPHOR uses exponential and de Vaucouleur fluxes from CModel), but because the measurements are done using the same pixels, these measurements are strongly correlated. The random flux perturbation is no longer valid and we find that the resultant photo- z 's have weird features. We thus resort to the COSMOS Wide-depth stacks. Thanks to a large number of visits available in the field, we could generate stacks with three different seeing FWHMs (0.5, 0.7 and 1.0 arcsec), which we will later use to evaluate the seeing dependence. We call these stacks the Wide-depth 'best', 'median', and 'worst' seeing stacks. Because we use only a small subsample of the UltraDeep COSMOS data (typically 1/10 of all the visits), it is reasonable to assume that the photometry is quasi-independent from the training sample. But, again, we urge caution when interpreting the absolute numbers. We note that the Wide-depth stacks have the same $N(z)$ distribution as the training sample, leading to some drawbacks we will discuss in Section 6.1. The COSMOS wide-depth stacks are included in the public data release (Aihara et al. 2017) and can be exploited by the community.

We note that the current Wide-depth stacks have a known issue that the i -band in the median seeing stack is slightly shallower than the Wide-depth (15min in total as opposed to the nominal exposure of 20min). But, for the purpose of photo- z analyses in this paper, we do not suffer significantly from this issue because we limit ourselves to relatively bright magnitudes of $i < 25$. Also, the slightly shallower depth only in one of the five bands does not have a major impact on the overall photo- z

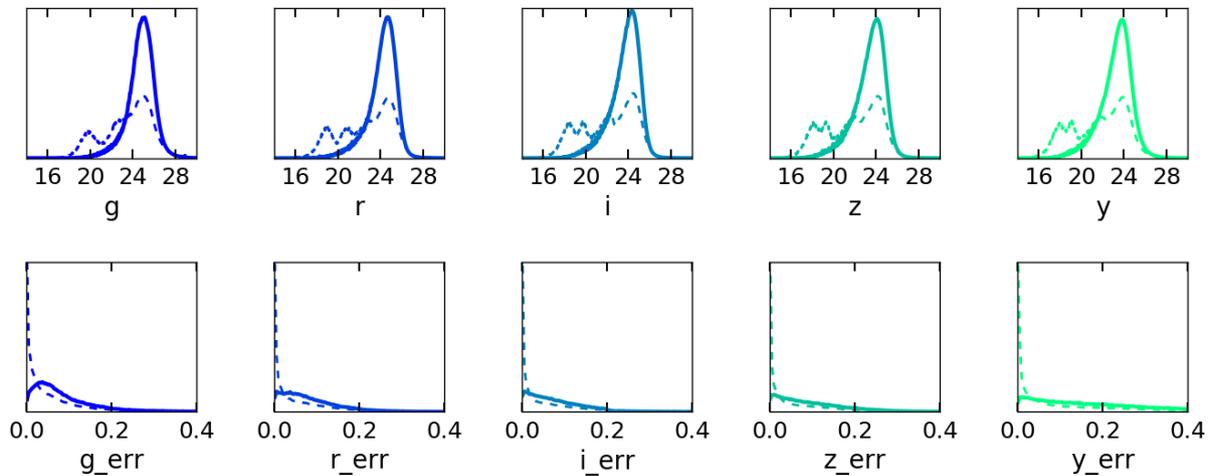


Fig. 1. The original (dashed) and re-weighted (solid) normalized number densities of our training sample as a function of *grizy* (left-to-right) magnitude (top) and error (bottom). Note that we use asinh magnitudes (i.e., Luptitudes) here. Our color-magnitude weights are able to effectively correct for biases in our original training sample to better mimic the HSC-SSP Wide data.

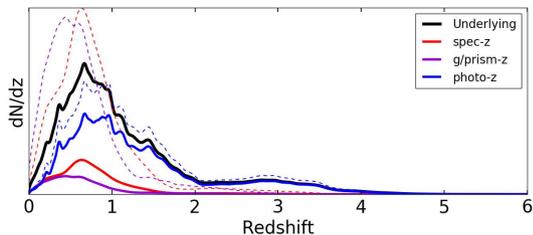


Fig. 2. The re-weighted, normalized redshift number density for our training sample. The full distribution is shown in solid black while the spec- z , g/prism- z , and many-band photo- z components are shown in solid red, purple, and blue, respectively. The dashed lines show these same components re-normalized to the full sample in order to better highlight their differences. We can see that most of the substructure in the redshift distribution of our training sample comes from the many-band COSMOS photo- z 's, which also contribute almost all of our high- z sources.

performance.

3 Methods

As we reviewed in the introduction section, each photo- z technique has pros and cons. For HSC-SSP, we use all the template fitting, empirical fitting, and machine-learning techniques to cover the wide range of scientific applications. We describe each of our code in this Section.

3.1 DEmP

The Direct Empirical Photometric code (DEmP; Hsieh & Yee 2014) is the successor of the empirical quadratic polynomial photometric redshift fitting code (Hsieh et al. 2005) applied to the Red-Sequence Cluster Survey data. DEmP is designed to minimize major issues of conventional empirical-fitting methods, e.g., how to choose a proper form of the fitting functions,

and biased results due to the population distribution of the training set, by introducing two techniques: regional polynomial fitting and uniformly weighted training set. The former is to perform fitting for each input galaxy using a subset of the training set galaxies with photometry and colors closest to those of the input galaxy, and the latter is to resample the training set to produce a flat population distribution. However, we find that using a uniformly weighted training set does not improve the overall photo- z quality. This is because the number density of this training set is sufficiently high thanks to the many-band photo- z 's from COSMOS; the subset of the training set used in the regional polynomial fitting consists of galaxies with very similar magnitudes and colors, which reduces the bias caused by the population distribution of the training set. Therefore, we use only the regional polynomial fitting to derive the HSC photo- z 's.

The probability distribution of photo- z for each galaxy is generated using Monte Carlo technique and the bootstrapping method. We use Monte Carlo technique to generate 500 data sets based on the photometry and uncertainties of the input galaxies to account for the effects due to photometric uncertainties. We then bootstrap the training set for each input galaxy 500 times for each of the Monte Carlo generated data set, to estimate the sampling effect in the training set. More details are described in Hsieh & Yee (2014). We use the PSF-matched aperture photometry (a.k.a. the *afterburner* photometry; Aihara et al. 2017) to derive photo- z 's for all the primary objects even with only one-band detection.

3.2 Ephor

Extended Photometric redshift (EPHOR) is a publicly available, neural network photo- z code¹. We use a feedforward neural network that has an input layer (\mathbf{x}_0), a series of hidden layers (\mathbf{x}_i for $i = 1, \dots, n$) and an output layer (\mathbf{y}). Variables with the bold typeface are horizontal vectors.

We feed the neural network with two model fluxes; de Vaucouleur flux and exponential flux in each band. These are derived as part of the CModel photometry (Bosch et al. 2017). The fluxes f_k are normalized before being fed to the neural network:

$$(\mathbf{x}_0)_k = \operatorname{arsinh}\left(\frac{f_k - \mu_k}{\sigma_k}\right), \quad (1)$$

in which μ_k is the median of f_k over the training dataset (training as opposed to validation and test), and σ_k is the interquartile range, non-normalized, of the training dataset. arsinh is applied so that unusually large fluxes will not ruin the neural network.

The hidden layers employ softplus ($\operatorname{softplus}(x) = \ln(1 + e^x)$) as the activation function:

$$\mathbf{x}_i = \operatorname{softplus}(\mathbf{x}_{i-1}W_i + \mathbf{b}_i) \quad \text{for } i = 1, \dots, n, \quad (2)$$

where W_i is a weight matrix and \mathbf{b}_i is a bias vector, both of which are determined in the training. The softplus activation function is applied to the argument vector elementwise. The neural network performs slightly better with softplus than with the rectifier $f(x) = \max(0, x)$.

The output layer is softmax: $\mathbf{y} = \sigma(\mathbf{x}_n)$, or

$$y_k = \left(\sigma(\mathbf{x}_n)\right)_k = \frac{e^{(\mathbf{x}_n)_k}}{\sum_{\ell} e^{(\mathbf{x}_n)_\ell}}. \quad (3)$$

We split the range of redshifts at equal intervals $z_0 < z_1 < \dots < z_d$, and equate y_k with the probability of the redshift being within the k -th bin $[z_{k-1}, z_k)$. We train the neural network by means of ADAM (Kingma & Ba 2014) so that the cross entropy defined below is minimized:

$$H = \left\langle -\sum_{k=1}^d y'_k \ln y_k \right\rangle, \quad (4)$$

in which the average is taken from the training dataset, and $\mathbf{y}' = (0 \dots 0 \ 1 \ 0 \dots 0)$ is a one-hot vector for a sample:

$$y'_k = \begin{cases} 1 & \text{if the sample's redshift is in } [z_{k-1}, z_k), \\ 0 & \text{otherwise.} \end{cases} \quad (5)$$

The default setup of EPHOR is to use the two model fluxes in each filter. But, we also run the code using the PSF-matched aperture photometry (one flux in each band) and we refer to the photo- z 's as EPHOR_AB. AB stands for afterburner.

3.3 FRANKEN-Z

Flexible Regression over Associated Neighbors with Kernel dENsity estimation for Redshifts (FRANKEN-Z) is a hybrid approach that combines the data-driven nature of machine learning with the statistical rigor of posterior-driven (i.e. template-fitting) approaches. Using machine learning, FRANKEN-Z attempts to approximate the ‘flux projection’ from a set of unknown target objects to a corresponding set of training objects in the presence of observational errors within both datasets. The corresponding mapping to redshift is then computed by stacking each training object’s posterior-weighted redshift kernel density estimate (KDE). This constitutes a generalization of typical template-fitting approaches to the machine-learning regime.

For the HSC-SSP PDR1, we approximated the associated flux projection using a collection of an object’s nearest neighbors in magnitude space. We incorporated observational errors by selecting object neighbors to be the union of the 10 nearest-neighbors in magnitude space computed using the PSF-matched photometry over 25 Monte Carlo realizations. The log-likelihoods for each object i given training object j were then computed using the associated fluxes via

$$-2 \ln P(i|j) = \sum_b \frac{(F_{i,b} - F_{j,b})^2}{\sigma_{i,b}^2 + \sigma_{j,b}^2} - n(i,j), \quad (6)$$

where the sum is taken over all bands indexed by b and $n(i,j)$ is the number of bands where both i and j are observed.

Because our nearest-neighbor search is in flux rather than redshift, our results are (somewhat) more robust to domain mismatches between the training/target datasets. We thus assume our prior is uniform over our training data such that our posterior is directly proportional to our likelihood. The redshift PDF $P(z|i)$ then constitutes a posterior-weighted sum

$$P(z|i) = \sum_j P(z,j|i) = \sum_j P(z|j)P(j|i) \propto \sum_j P(z|j)P(i|j) \quad (7)$$

where $P(j|i)$ is the posterior and $P(i|j)$ is again the likelihood.

We note that the full code is still under active development and is more flexible than the early version utilized here. It can be found at <https://github.com/joshspeagle/frankenz>. See Speagle et al. (in prep.) for additional details.

3.4 MLZ

SOMz is a part of the public photo- z code, MLZ, which enables us to estimate photometric redshift with *Self-Organizing Map* (SOM). The SOM algorithm itself is an unsupervised machine learning method and is widely used to classify a given dataset into small segments with similar properties. For photo- z measurements, we first apply the SOM to the training set and assign a redshift to each segment by computing the mean redshift of the galaxies in that segment. Then, we find the closest segment for every photometric objects to assign a redshift. Monte-Carlo

¹ <https://hsc-release.mtk.nao.ac.jp/doc/index.php/photometric-redshifts/>

and bootstrap resampling enables us to produce the probability distribution of every galaxy.

We describe each step in more detail. First we prepare the random map of N_{pix} defined on a 2-dimensional sphere, where pixel is defined by Healpix pixelization with $N_{\text{pix}} = 12 \times N_{\text{side}}^2$. The p -th pixel has a vector w_{pi} describing the object properties, e.g. 5-band magnitudes, where subscript p runs from 1 to N_{pix} , and $i = 1, 2, \dots, N_{\text{att}}$ with N_{att} being the number of properties to characterize objects, i.e. k -th galaxy has data vector $x_k = \{x_{1k}, x_{2k}, \dots, x_{N_{\text{att}}k}\}$. Here we utilize 5 band magnitudes of CModel photometry, and 10 colors derived from those magnitudes. During the optimization, we find that colors from afterburner photometry in addition to CModel magnitudes and colors, slightly improve the photo- z performance. Therefore, we characterize objects with 5+10+10 attributes with their measurement errors. Not all the attributes are independent and there are covariances between them. We ignore the covariances for now and leave it to our future work to evaluate their effects on photo- z 's.

As an initial condition of the map, we set the vector value in each pixel randomly drawn from the data vector. The Euclidean distance between a given galaxy and pixel is defined as

$$d(p, k) = \sqrt{\sum_i \frac{(w_{pi} - x_{ik})^2}{\sigma_{ik}^2}}. \quad (8)$$

Then we look for the nearest pixel for the given galaxy. For the nearest pixel of the k -th galaxy $\hat{p}(k)$, $d(\hat{p}, k) \leq d(p, k)$ holds for any p . The weight vectors of the nearest pixel and the vicinity of the nearest pixels are iteratively updated as,

$$\mathbf{w}_p(t+1) = \mathbf{w}_p(t) + \alpha(t) \exp\left[-\frac{\gamma^2(p, \hat{p})}{2\sigma^2(t)}\right], \quad (9)$$

where $\gamma(p, \hat{p})$ is the angular distance between pixel p and the nearest pixel \hat{p} and α, σ are monotonically decreasing functions with time t . The time t increases by 1 after we use one galaxy. After the pixels are updated using all galaxies, the same processes are iteratively applied except for setting the initial map to be random. We iterate this for N_{ite} times. In order to obtain a reliable redshift probability distribution function, $P(z)$, we make a perturbed catalog using both bootstrap resampling and Monte-Carlo methods. For the latter, we perturb all the magnitudes and colors according to their measurement errors. As a result, we have $N_{\text{boot}} \times N_{\text{MC}}$ samples to derive our final $P(z)$.

As described in Section 2.2, we optimize the hyper-parameters using fold 1-3 and evaluate the performance with fold 4. We note that the optimization is performed in terms of minimizing the σ_{conv} instead of *loss* function introduced in Section 4.1. That might partly be the reason why the MLZ performed worse than other machine-learning codes, as we discuss later. The hyper-parameters include N_{pix} , N_{att} , N_{ite} , N_{boot} and N_{MC} . Given the reasonable timescale to compute a large number of objects, we find out the optimal hyper-parameter set

as $N_{\text{pix}} = 16$, $N_{\text{att}} = 5 + 10 + 10 = 25$, $N_{\text{ite}} = 200$, $N_{\text{boot}} = 24$ and $N_{\text{MC}} = 16$. Except for the N_{att} , the increase of those parameters do not significantly improve our results.

3.5 NNPZ

Nearest Neighbors P(z) (NNPZ) redshifts are computed following the method introduced by Cunha et al. (2009). The principle of the method is explained in their Section 2.2 and can be summarized as finding the nearest neighbors around an unknown object in the Euclidian color/magnitude space from a reference sample and using the reference redshift histogram as the PDF. There exists, however, a number of differences between the original method and the one applied here:

- $i, g-r, r-i, i-z, z-y$ color/magnitude attributes (CModel photometry) are used.
- The reference sample is the weighted training sample (fold 1-3) as described in Section 2.
- The neighbors are weighted according to the inverse Euclidean distance in the color/magnitude space.
- To avoid giving too much weight to a neighbor with low signal-to-noise photometry that accidentally lies very close to the target object, the neighbors with large photometric errors are down-weighted. To do so, we first compute a photometric-error estimate as the sum of the photometric errors in all bands from both the unknown and neighbor objects, and we take the inverse of the photometric-error estimate as the weight.

The final weight for each neighbor is the product of the reference, distance and photometric-error weights. The final object $P(z)$ is thus the weighted histogram of the neighbors. We also record the neighbor redshifts and weights in additional output tables. We note that the choice of maximum number of neighbors, here 50, has little impact owing to the weighting scheme in color/magnitude space. We do not produce a $P(z)$ when the CModel measurement has failed in any of the bands.

3.6 Mizuki

Finally, we use a template fitting-code MIZUKI (Tanaka 2015). This code differs from classical template fitting codes in a few respects. It uses a set of templates generated with the Bruzual & Charlot (2003) stellar population synthesis code assuming a Chabrier (2003) IMF and Calzetti et al. (2000) dust attenuation curve. Emission lines are added to the templates assuming solar metallicity (Inoue 2011).

There are pros and cons in using stellar population synthesis models. One disadvantage of using theoretical templates is that they deliver less accurate photometric redshifts than empirical templates because empirical templates often fit the observed SEDs of galaxies better. However, we correct for this template

mismatch by applying a template error function (Brammer et al. 2008), which comes in two terms both as a function of rest-frame wavelength. One is a systematic flux correction applied to the templates to reduce the mismatch and the other is template flux uncertainty to properly weight (un)reliable parts of SEDs. This template error function can be derived from the data by comparing the best-fit model fluxes and the observed fluxes of objects. We use the training sample (fold 1-3) to generate the template error function.

A big advantage of using theoretical templates is that we know the physical properties of galaxies such as SFR and stellar mass for each template. We apply a set of Bayesian priors on the physical properties and let the priors depend on redshift. Refer to Tanaka (2015) for details of the priors, but they are all observationally motivated. What these priors effectively do is (1) to keep the template parameters within realistic ranges to reduce the degeneracy in the multi-color space and also (2) to let templates evolve with redshift in an observationally motivated way. Both template error function and the physical priors improve photometric redshifts. An improvement to the original code is that the $N(z|mag)$ prior is extended to multi-color space and it now uses $N(z|g-i, i-y, i)$. We make grids in the two-color magnitude space and pre-compute $N(z)$ in each grid using the training sample (fold 1-3). There are some redshift spikes in the COSMOS field and we apply Gaussian smoothing with $\sigma_z = 0.05$ in each grid to largely smear out the COSMOS-specific features. In addition to redshifts, we compute stellar mass, SFR, and extinction fully marginalized over all the other parameters, which can be useful for galaxy science. Appendix 2 compares stellar mass and SFRs from the code against an external multi-wavelength survey.

In addition to galaxy templates, we also include QSO/AGN templates and stellar templates. The QSO/AGN templates are generated by combining the type-1 QSO spectrum from Polletta et al. (2007) and young galaxy templates from Bruzual & Charlot (2003) assuming $\tau = 1\text{Gyr}$, $\text{age} < 2\text{Gyr}$, and $0 < \tau_V < 2$, where τ is an exponential decay timescale of star formation history, age is time since the onset of star formation, and τ_V is the optical depth (attenuation) in the V -band. The relative fractions of the QSO and galaxy components are 0.5:1, 1:1, 2:1, and 4:1. These hybrid templates are similar to those presented in Salvato et al. (2009). For the stellar templates, we use BaSeL 3.1 stellar library (Westera et al. 2002). These QSO and stellar templates are used to give relative probabilities of objects being galaxy, QSO, or star. At this point, this functionality of the code is still preliminary, and for simplicity, we use stellar and QSO templates for compact sources (we use the standard extendedness parameter from the pipeline down to $i \sim 24$ to identify compact objects and all the fainter objects are assumed to be extended; see Aihara et al. 2017 for details). Only the galaxy templates are used for extended sources.

One important caveat in this release is that the code is trained using an old version of the training sample with erroneous weights (the one described in Section 2.1 but without the `centroid_sdss` flag cut). We unfortunately did not have time to re-train the code with the new training sample. This might be part of the reason why the code performs worse than the other codes.

4 Metrics and Their Definitions

4.1 Metrics to characterize photo- z

There are a few standard quantities used to characterize photo- z accuracy. However, as their definitions are not always the same in the literature, we explicitly define them here for this paper. We also introduce new quantities.

- **Bias:** Photo- z 's may systematically be off from spectroscopic redshifts and we call this systematic offset bias. We compute a systematic bias in $\Delta z = (z_{\text{phot}} - z_{\text{ref}})/(1 + z_{\text{ref}})$ by applying the biweight statistics (Beers et al. 1990). The biweight is a robust statistical method to estimate the center and dispersion of a data sample by applying a weight function to down-weight outliers, which we often have in photo- z 's. We iteratively apply 3σ clipping for 3 times to further reduce outliers.

- **Dispersion:** In the literature, dispersion is often computed as

$$\sigma_{\text{conv}} = 1.48 \times \text{MAD}(\Delta z), \quad (10)$$

where MAD is the median absolute deviation. Note that this definition does not account for the systematic bias. In addition to this conventional definition, we also measure the dispersion by accounting for the bias using the biweight statistics. We iteratively apply a 3σ clipping as done for bias to measure the dispersion around the central value. We denote the conventional dispersion and the biweight dispersion as σ_{conv} and σ , respectively.

- **Outlier rate:** The conventional definition is

$$f_{\text{outlier,conv}} = \frac{N(|\Delta z| > 0.15)}{N_{\text{total}}}, \quad (11)$$

where outliers are defined as $|\Delta z| > 0.15$. Again, this definition does not account for the systematic bias. The threshold of 0.15 is an arbitrary value but is probably reasonable for photo- z 's with several bands. It is clearly too large for those with many bands. Together with this conventional one, we also define outliers as those 2σ away from the central value (these σ and center are from biweight; see above). This 2σ is an arbitrary choice, but it is motivated to match reasonably well with the conventional one for several band photo- z 's. We will denote the σ -based outlier fraction as f_{outlier} and the conventional one as $f_{\text{outlier,conv}}$.

- **Loss function:** It can be cumbersome to use multiple indicators to characterize the photo- z accuracy. Here we define a simple loss function to remedy the complexity and help us

capture the photo- z accuracy with a single number. We define a loss function as

$$L(\Delta z) = 1 - \frac{1}{1 + \left(\frac{\Delta z}{\gamma}\right)^2}. \quad (12)$$

This is an 'inverted' Lorentz function. The loss is zero when $\Delta z = 0$ and continuously increases with larger Δz . Thus, this can be considered as a continuous form of the outlier rate defined above. The loss also increases with the photo- z bias because a systematic bias means non-zero Δz for most objects. The loss also increases with dispersion because a larger dispersion means larger Δz . Therefore, it effectively combines the three popular metrics into a single number. In order to keep a rough consistency with the conventional outlier definition, we adopt $\gamma = 0.15$.

4.2 Optimal point estimates and photo- z risk parameter

Our photo- z methods do not output a point redshift directly, but instead infer a redshift PDF, $P(z)$. We want to use the full $P(z)$ for science, but it is often useful to reduce the PDF to a point estimate, z_{phot} . There are several ways to do it; the mean, median or mode of $P(z)$, for example. To obtain the "best" point estimate, however, we take the *minimum risk* strategy — we define a "risk" parameter as a function of redshift and choose the point where the risk is minimized as the best point estimate.

The loss function $L(\Delta z)$ defined above is a function of z_{phot} and z_{ref} , and can be viewed as a loss arising from z_{phot} being different from z_{ref} . The expected amount of loss for a point estimate z_{phot} can be estimated as

$$R(z_{\text{phot}}) = \int dz P(z) L\left(\frac{z_{\text{phot}} - z}{1 + z}\right). \quad (13)$$

The integral $R(z_{\text{phot}})$ depends only on z_{phot} and represents the expected loss for a given choice of z_{phot} as the point estimate. We employ $R(z_{\text{phot}})$ as the "risk" function. The risk $R(z_{\text{phot}})$ can be roughly interpreted as the probability of the inferred redshift z_{phot} being an outlier: the loss $L(\Delta z)$ is approximately 0 if the guess z_{phot} is close to the true answer z_{ref} , and it is approximately 1 if the guess z_{phot} differs largely from the true answer z_{ref} .

As mentioned above, we take the minimum risk strategy to choose a point estimate z_{phot} at which the risk $R(z_{\text{phot}})$ is minimum, which we call the *best* point estimate z_{best} :

$$z_{\text{best}} = \text{argmin}(R(z_{\text{phot}})). \quad (14)$$

This minimal point has no closed-form solution and must be searched for numerically.

In addition to z_{best} , we also compute z_{mean} , z_{mode} , and z_{median} and make comparisons between them in the next section, where we demonstrate that z_{best} indeed performs best.

Equally important to the point estimate is the reliability of the point estimate, and we naturally use the risk parameter, $R(z_{\text{phot}})$, for this². We compute the risk parameter for each point estimate (e.g., $R(z_{\text{mean}})$). To facilitate comparisons to previous work, we also compute the commonly used estimator of redshift confidence, $C(z)$, defined as

$$C(z_{\text{phot}}) = \int_{z_{\text{phot}}-0.03}^{z_{\text{phot}}+0.03} P(z) dz, \quad (15)$$

where z_{phot} is a point estimate such as median and best. This is primarily to keep consistency with previous studies, since we will show later that $R(z_{\text{phot}})$ is a better estimator of photo- z reliability.

5 Performance Evaluation Using Point Estimates

We now characterize the performance of our photo- z 's. We first evaluate how well the 'best' point estimator works compared to other popular statistics. We then move on to show our photo- z accuracy at the Wide depth, followed by discussions on the depth and seeing dependence of the accuracy. We focus on the point estimator to characterize our photo- z performance in this section. We present PDF-based tests in Section 6.

5.1 The 'best' point estimate

One of the most popular point estimators used for photo- z is the median, which is defined as the redshift at which the integrated probability equals 0.5. The mode of PDF is also frequently used. We compare the mean, mode, median, and best redshifts using the COSMOS Wide-depth median seeing stack (see the next section for details) for MLZ in Table 1. We use all galaxies with $i < 25$ here. The best estimator gives the smallest scatter and lowest outlier rate³ compared to the other estimators. The best estimator tends to introduce a small negative bias, but the bias is not sufficiently large to prevent most scientific applications. The other photo- z codes show the same trend. Based on this result, we will use the best estimator in what follows and denote the best redshift as z_{phot} for simplicity.

5.2 Photo- z performance at the Wide-depth

We characterize the photo- z performance at the Wide-depth, representative depth of the HSC survey as a whole, using the metrics defined in Section 4. We compare z_{phot} with z_{ref} for the COSMOS Wide-depth median seeing stack. Recall that this is a subsample of UltraDeep COSMOS data stacked to the depth

² In the catalog database at the data release site, this parameter is named `photoz_risk`.

³ f_{outlier} is larger for best than for median, but it is due to reduced scatter (σ). Recall that f_{outlier} is defined as 2σ outliers.

Point Estimator	bias	σ_{conv}	$f_{outlier,conv}$	σ	$f_{outlier}$	loss
mean	-0.003	0.075	0.227	0.078	0.218	0.260
mode	-0.002	0.067	0.213	0.064	0.240	0.244
median	-0.001	0.066	0.199	0.064	0.226	0.236
best	-0.003	0.064	0.197	0.061	0.229	0.233

Table 1. Photo- z performance using mean, mode, median, and best estimators. The numbers are for MLZ, but all the other codes show the same trend.

of the Wide survey and all the filters have 0.7 arcsec seeing. Fig. 3 shows the bias, scatter and outlier fraction as a function of i -band magnitude for all the codes. More statistics are summarized in Table 2. Most of the reference redshifts at faint magnitudes come from the COSMOS photo- z catalog and they are not very accurate at $i \gtrsim 25$. We thus cut at $i = 25$ and characterize the performance at brighter mags. Once again, not all the COSMOS photo- z 's are correct and we inherit the systematic uncertainty from COSMOS. The absolute numbers of the statistics shown in the figure should thus be taken with caution.

Before we compare the codes, it is important to note that we observe a sign of over-fitting in FRANKEN-Z even though the COSMOS Wide-depth stacks were not explicitly included during the training. This is likely due to FRANKEN-Z's sensitivity to both the redshift PDF and error distributions in both datasets, which makes it more sensitive to our assumption that the two datasets are quasi-independent (see section 6 for details). It is thus unfair to compare its performance directly with the other codes, since it is likely to be overly optimistic.

The photo- z accuracy is a strong function of magnitude, but it is relatively flat down to $i \sim 23$ for all the codes. The scatter and outlier rate are about 0.03 and 5%, respectively, at this bright mags. This flat performance is likely because most objects within this magnitude range are located at $z \lesssim 1.5$, where we can obtain fairly good photo- z 's with the *grizy* photometry (see below). At fainter mags, the fraction of $z > 1.5$ objects increases and these high redshift galaxies drive the poor performance at faint mags. It is encouraging that the bias is still within $\sim 1\%$ at all mags for most codes.

Fig. 4 shows the same metrics but as a function of z_{phot} . Our performance is poor both at low- z ($z \lesssim 0.2$) and high- z ($z \gtrsim 1.5$) ends. This is expected because our filter set (*grizy*) does not straddle the 4000Å break at these redshifts. We are not able to break the degeneracy between $z \sim 0$ and $z \sim 2$ solutions (i.e., 4000Å break and Lyman break degeneracy), resulting in poor performance at low- z . At $z \gtrsim 1.5$, we probe only the featureless UV continuum and it makes it difficult to obtain good photo- z 's there. The Lyman break comes in the g -band and some codes show improvements at $z \gtrsim 3.5$. In the good redshift range ($0.2 \lesssim z \lesssim 1.5$), our photo- z 's are fair – the outlier rate is about 15% and the scatter is about 0.05. Note that these numbers are for all galaxies down to $i = 25$. If we use

brighter galaxies with $i < 24$, the numbers improve to about 8% and 0.04. Our photo- z 's should thus be sufficient to enable many of the science goals in HSC-SSP. Also, we can clip potential photo- z outliers to further improve the accuracy (see Section 5.5). Table 3 summarizes the statistical measures for all the codes.

5.3 Code-code comparisons

In the previous subsection, we plot the three metrics (bias, dispersion, and outlier rate) separately for each code. But, it is useful to use a single metric to compare the performance between the codes. For this, we use the loss parameter, $L(\Delta z)$, introduced earlier. Because this is not a popular statistic used in the literature, we first show its relationship between the other statistical measures in Fig. 5. The figure is for MLZ, but the other codes behave similarly. While all of the bias, scatter and outlier rate are correlated (all of them get worse at fainter magnitudes), it is clear that the mean loss most strongly correlates with the outlier rate. Loss should also change with bias and scatter at fixed outlier rate by definition, but it is the outlier rate that increases drastically at faint mags and the mean loss most strongly correlates with that parameter.

Figs. 6 and 7 shows the mean loss as a function of magnitude and z_{phot} , respectively. All the codes show a similar behavior in these figures; the accuracy starts to get worse around $i = 23$ and the redshift range of $0.2 \lesssim z \lesssim 1.5$ shows the best performance. Mizuki tends to perform worse than the other codes. Although it was trained on an earlier version of the training sample with sub-optimal weights (see Section 3.6), it is the only classical template-fitting code and it might suggest that machine-learning codes outperform template fitting. There are advantages and disadvantages in both techniques and we will discuss them further in Section 8. Again, note that the metrics for FRANKEN-Z are likely overly optimistic given some degree of over-fitting.

5.4 Seeing and depth dependence

The photometric accuracy is not only a function of integration time and sky transparency, but also seeing. As described in Section 2.3, we have generated the COSMOS wide-depth stacks for three different seeing FWHMs. We use them to evaluate the seeing dependence of our photo- z accuracy at the Wide-depth.

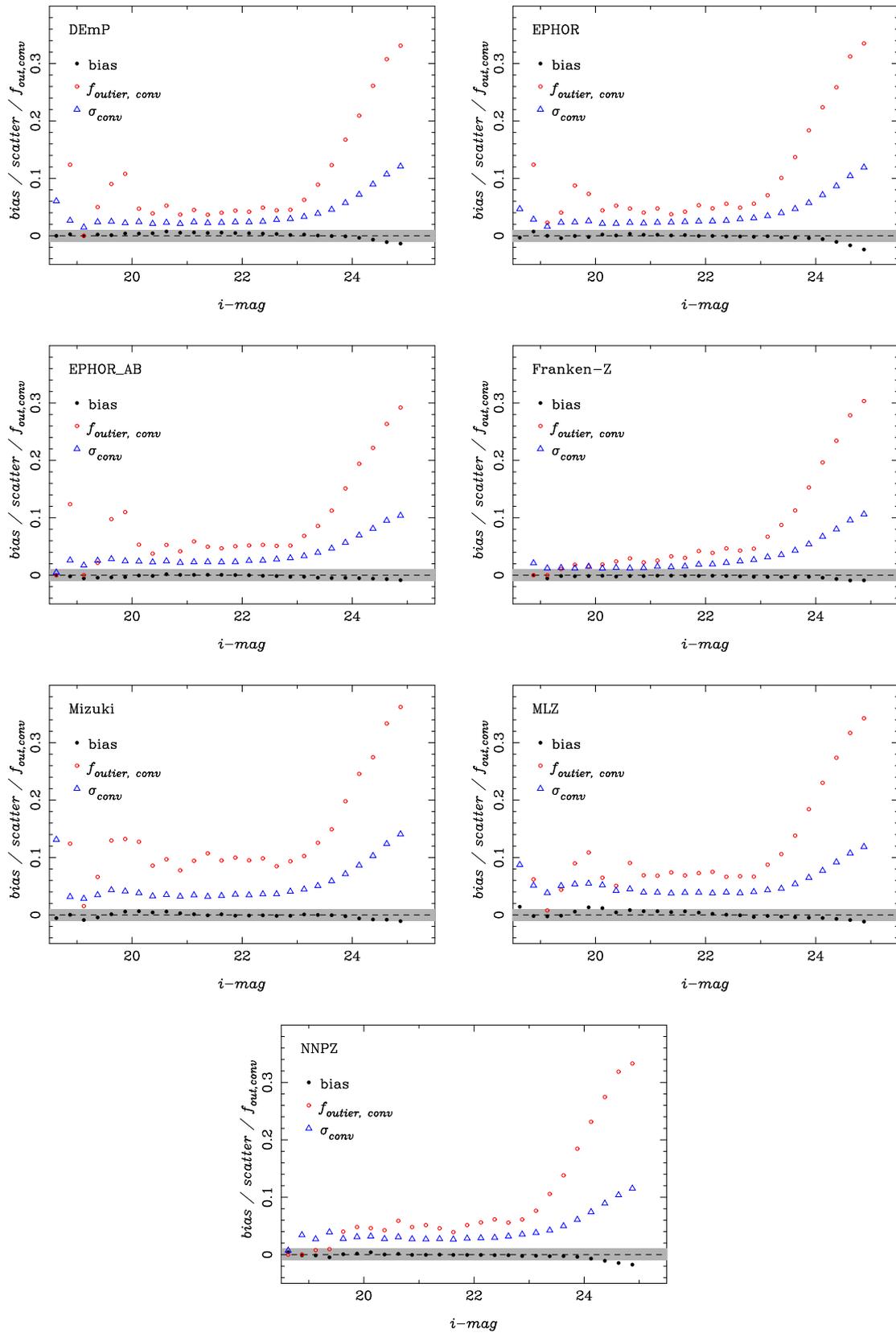


Fig. 3. Bias, $f_{\text{outier,conv}}$ and σ_{conv} plotted against i -band magnitude. The different panels are for different codes as indicated by the label on the top-left corner of each panel. The gray shades show ± 0.01 range, which will be useful for bias. The symbols are explained in the panels. Note that these plots are based on the COSMOS Wide-depth median stack and include objects in COSMOS only.

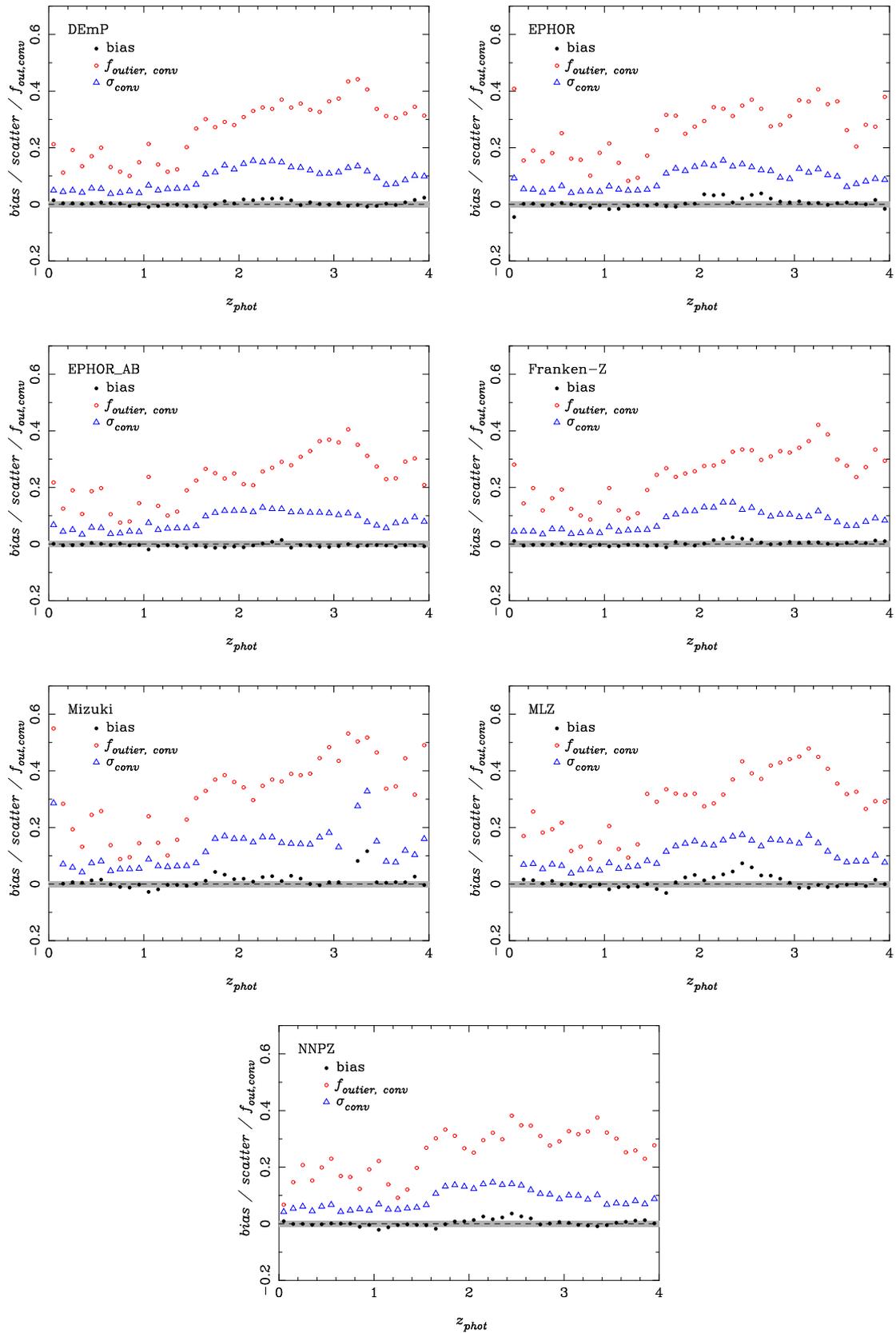


Fig. 4. Same as Fig. 3 but as a function of z_{phot} .

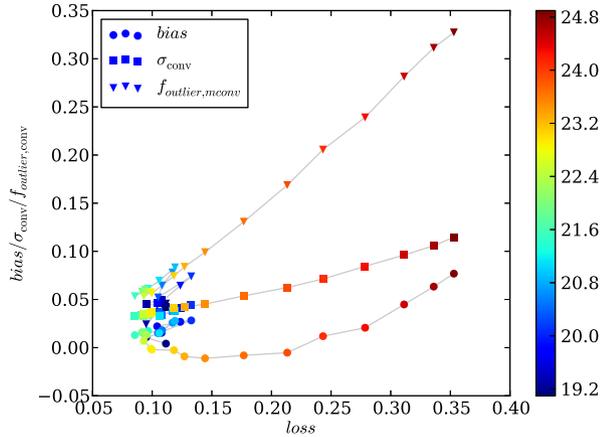


Fig. 5. Relationship between loss and other metrics. The symbols are color-coded according to the i -band magnitude cut applied. This is for MLZ using the Wide-depth median seeing catalog, but the other codes show similar trends.

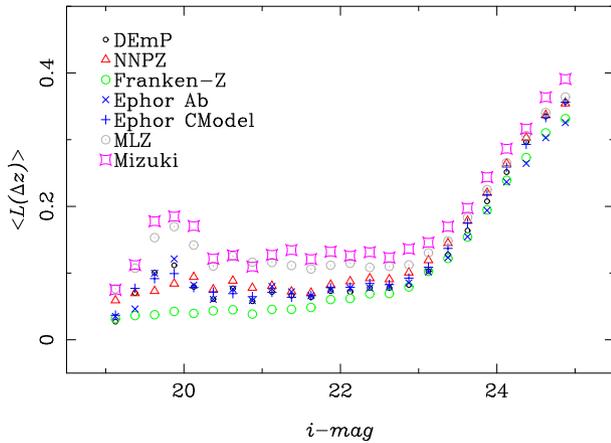


Fig. 6. Mean loss as a function of i -band magnitude for all the codes. The symbols are explained in the figure.

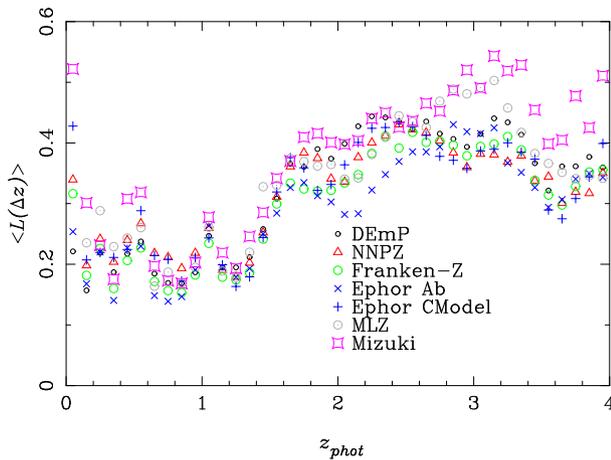


Fig. 7. Same as Fig. 6 but as a function of z_{phot} .

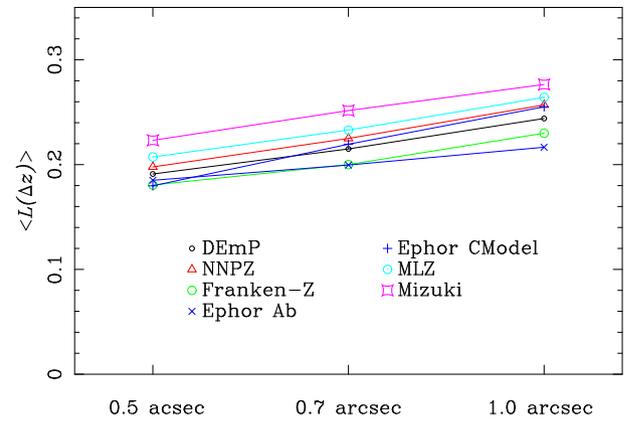


Fig. 8. Mean loss as a function of seeing.

Fig. 8 shows $\langle L(\Delta z) \rangle$ as a function of seeing. Loss is larger at worse seeing as expected and we find $\Delta \langle L(\Delta z) \rangle \sim 0.05$ between the two extremes. Most of the HSC data are taken under 0.5 – 1.0 arcsec seeing (Aihara et al. 2017), and Fig. 8 gives the peak-peak variation of our photo- z performance across the Wide survey. EPHOR delivers photo- z 's computed with CModel and PSF-matched aperture photometry (EPHOR and EPHOR_AB, respectively). A comparison between them show how strongly each photometry technique suffers from the seeing variation. The PSF-matched photometry turns out to be less strongly affected by seeing than CModel; $\Delta \langle L(\Delta z) \rangle \sim 0.03$ and 0.06 for PSF-matched and CModel photometry, respectively. The weaker seeing dependence of the PSF-matched photometry is not surprising because the images are smoothed to 1.1 arcsec FWHM, regardless of the native seeing. It is, however, rather surprising that the measurements under the native seeing deliver poorer photo- z accuracy. But, we note that the current CModel has issues with a prior, which affects the resultant photometry (Bosch et al. 2017; Huang et al. 2017). It is unlikely that the color measurements are severely affected, but fluxes are undoubtedly affected. Also, the deblending algorithm tends to fail in dense regions such as cluster cores (Aihara et al. 2017), which also affects CModel measurements. The PSF-matched photometry suffers less from the deblending issue because it is performed without deblending. Future improvements in the measurement algorithms will make CModel work better.

The depth dependence is shown in Fig. 9. Again, all the codes behave similarly and the mean loss is smaller by ~ 0.1 at the UltraDeep depth. Although not shown in the figure, the improvement is not limited to $0.2 < z < 1.5$ but is observed at all redshifts. This implies that obtaining photometry in more filters is not the only way to improve photo- z 's. Going deeper can be a useful alternative.

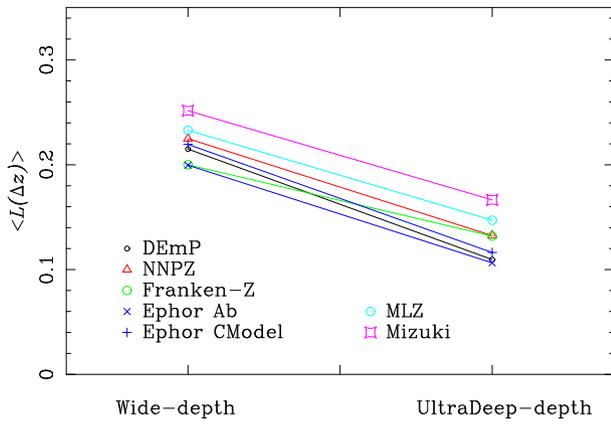


Fig. 9. Same as Fig. 8 but as a function of depth.

5.5 Cut on the risk parameter

We have characterized our photo- z performance using all galaxies down to $i = 25$ without any clipping of potential outliers. We can achieve reasonably good photo- z accuracy at a somewhat limited redshift range due to the filter set as discussed above. Also, our photo- z 's are of course not perfect and there are always outliers even within the good redshift range. There are a few quantities that can be used to indicate a reliability of photo- z such as $C(z)$ and odds (Benitez 2000) that allow us to remove potential outliers. We have introduced a new parameter, $R(z)$, in Section 4.2 and here we compare this new parameter with the commonly used $C(z)$.

Fig. 10 compares $C(z_{phot})$ and $R(z_{phot})$. As defined earlier, z_{phot} is the best point estimate. We remove objects with $C(z_{phot})/R(z_{phot})$ smaller/larger than a threshold value and plot the resultant $\langle L(\Delta z) \rangle$ as a function of the fraction of objects removed. At a given fraction of removed objects, $\langle L(\Delta z) \rangle$ is always smaller for $R(z_{phot})$ than for $C(z_{phot})$. For instance, at $f_{removed} = 0.5$ (i.e., we remove a half of the objects), which roughly corresponds to $C(z_{phot}) < 0.5$ and $R(z_{phot}) > 0.9$ cuts, loss is smaller for $R(z_{phot})$ by about 0.02. $R(z_{phot})$ is designed to minimize loss and thus this may not be a fair comparison, but we observe the same trend if we plot other quantities such as the outlier rate. This demonstrates that $R(z)$ works better at identifying outliers than the commonly used $C(z)$.

6 Accuracy of PDF

We have focused on the point statistics in the previous section. We now move on to discuss the accuracy of the full PDF. We first focus on the $N(z)$ distribution of galaxies and then turn our attention to Probability Integral Transform (PIT) and Continuous Ranked Probability Score (CRPS) to evaluate the PDF accuracy.

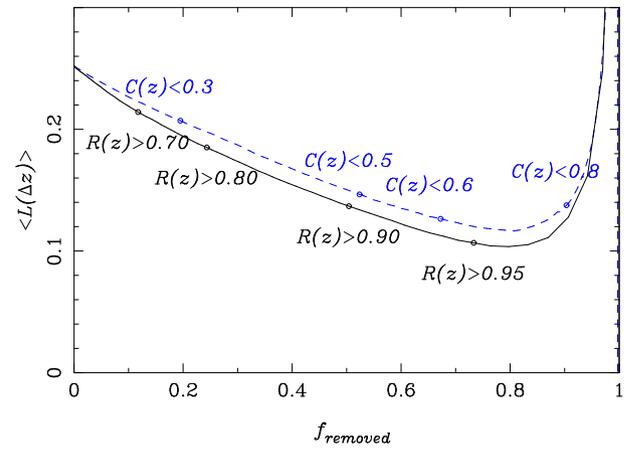


Fig. 10. Loss plotted against the fraction of objects removed by applying a cut on $C(z_{phot})$ and $R(z_{phot})$. z_{phot} is denoted as z in the figure for simplicity. The dashed and solid curves are for $C(z_{phot})$ and $R(z_{phot})$ and threshold applied for each of them are shown in the figure. This is for Mizuki, but the other codes show a similar trend.

6.1 $N(z)$ distribution

In various scientific uses, we often consider not only the redshift for single galaxy but also the global properties averaged over a number of objects. In this section, we show redshift distributions of photometric sample from the S16A internal release and compare them among the seven different photo- z codes.

6.1.1 Internal comparisons

As we will discuss in Section 7, we randomly draw a redshift from $P(z)$ for each object (z_{MC}). We first demonstrate that this Monte-Carlo draw from the PDF well reproduces the original PDF and is a very useful point estimate for a statistical sample. In Fig. 11, we compare the stacked PDF and the sum of z_{MC} using Gaussian Kernel Density Estimator (KDE),

$$N^P(z) = \frac{1}{n} \sum_i^n P_i(z) \quad (16)$$

$$N^{MC}(z) = \frac{1}{\sqrt{2\pi}nh} \sum_i^n \exp\left[-\frac{(z - z_{MC,i})^2}{2h^2}\right], \quad (17)$$

where the kernel width h is set to the PDF resolution, 0.05 for EPHOR and EPHOR_AB and 0.01 for all the other codes. The estimator reduces the discreteness of the sample, but we found that given the large number of objects, we do not see any major differences between the classical count-up histogram and KDE.

As shown in the figure, we see a good agreement between N^{MC} and N^P for most codes, although N^{MC} fails to trace small scale spiky features in NNPZ, EPHOR, EPHOR_AB seen in N^P . In the same figure, we also plot the $N(z)$ distribution from z_{best} using Eq. 17. Although the z_{best} is the optimal point estimate in terms of minimizing the risk function (see section 4.2), N^{best} amplifies the wiggle feature of the $N(z)$ distribution. This might imply that the point estimates are affected by

inhomogeneities in the training sample. For instance, the local peaks around $z \sim 1.5$ are a consequence of the bumpy structure in the COSMOS 30-band photo- z , on which we highly rely to calibrate our photo- z 's (see also Fig. 13). N^{best} for Mizuki is least affected since the template fitting does not rely on the training sample very much, while machine learning codes do. In the following, we use N^{MC} as the representative of the redshift distribution instead of N^{P} since summing up the full PDF is computationally much more expensive.

Figure 12 shows the $N(z)$ distribution from z_{MC} for bright ($i < 22.5$) and faint ($i > 22.5$) sample. Sharp drop of bright sample at $z \sim 1$ reflects that we have few bright objects at $z > 1$. On the other hand, we have galaxies out to $z \sim 6$ in the fainter sample. Although there are subtle differences between the codes, the overall redshift distributions are similar for all of the codes, which is encouraging.

6.1.2 External comparisons

We have compared the internal consistency in the previous section. We now turn our attention to external comparisons using the reference redshifts in the COSMOS Wide-depth median stack. Fig. 13 shows the comparison between N^{MC} and $N(z)$ based on the reference redshifts. Assuming that the reference redshifts are correct, the deviations from their $N(z)$ is an indication of incorrect PDF. While all the codes reproduce the overall $N(z)$ reasonably well, NNPZ reproduces the $N(z)$ most accurately. Mizuki misses a peak at $z \sim 0.35$, and EPHOR, MLZ, and NNPZ tend to overestimate at $z \sim 0.7$. This has implications for weak-lensing science, which often relies on $N(z)$ from photo- z . However, detailed discussions of the over/underestimated $N(z)$ for weak-lensing are beyond the scope of the paper and can be found elsewhere (More et al. in prep.).

We have trained our codes using galaxies that are primarily from COSMOS especially at faint mags, and we have compared our $N(z)$ against COSMOS. Re-weighting the training galaxies to reproduce the HSC Wide sample largely eliminates the circularity here. However, it will certainly be useful to have a separate field with different $N(z)$ for more comparisons. Such a COSMOS-like field with accurate photo- z 's down to faint mags is currently not available, which is a one of the major limitations of our photo- z tests. We will discuss our future directions in Section 8.

6.2 Tests on PDF

As a further test of the accuracy of PDF, we apply two techniques; Probability Integral Transform (PIT) and Continuous Ranked Probability Score (CRPS). They are summarized in Polsterer et al. (2016), but a brief description is given here.

PIT was proposed as a visual diagnostic tool to check the calibration of PDF. It is a very simple diagnostic and one only

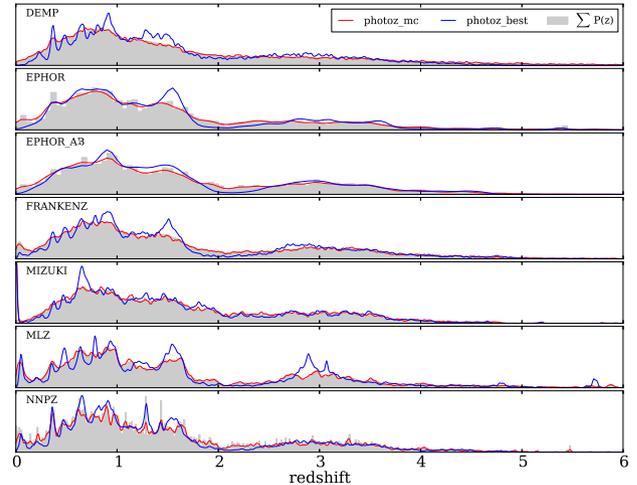


Fig. 11. $N(z)$ distributions for all galaxies in the Wide layer inferred using a few different estimators; sum of full PDF (gray histogram), Gaussian KDE for z_{MC} (red line) and z_{best} (blue line). Sum of full PDF and $N(z_{\text{MC}})$ agrees very well, while $N(z_{\text{best}})$ estimates show sharp redshift spikes. This is likely due to the spikes present in the training data from COSMOS.

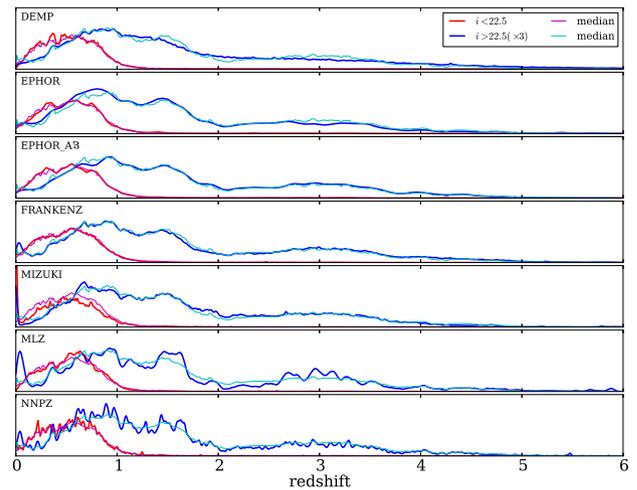


Fig. 12. $N(z)$ distribution for bright (red) and faint (blue) samples. The median distribution of all the photo- z codes are also shown for bright (magenta thin line) and faint (cyan thin line) samples. EPHOR looks smoother than the others due to a larger redshift bin size.

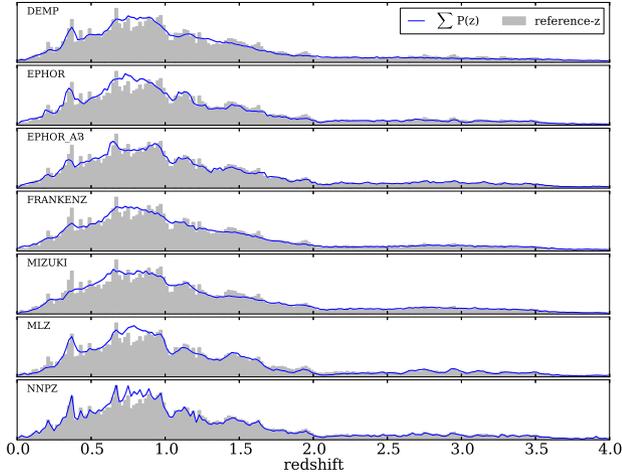


Fig. 13. $N(z)$ distributions from COSMOS wide depth stacked image with median seeing (blue lines) and reference redshifts (gray shaded histogram).

needs to draw a histogram of the following integrated probability,

$$PIT(z_{ref}) = \int_0^{z_{ref}} P(z) dz, \quad (18)$$

for all objects in the test sample. The left panels in Fig. 14 show the PIT histograms for all the codes. If the PDF is calibrated well, we expect to observe a flat PIT distribution. Deviations from the flat distribution is an indication of incorrect PDF and this formed a basis of the empirical PDF re-calibration by Bordoloi et al. (2010). EPHOR_AB shows a convex shape, which is a clear indication of overdispersed PDF, i.e., PDF is too wide. On the other hand, Mizuki has a concave shape and it indicates that the PDFs are underdispersed, i.e., PDF is too narrow. Most of the other codes show a relatively flat distribution, except at the two extremes of the distribution, where many codes show a spike. These spikes are caused by outliers and the figures suggest that the outliers are not properly captured in the PDFs.

FRANKEN-Z shows an interesting PIT distribution with a peak at the center. The peak indicates that a larger-than-expected fraction of objects have the median redshift almost exactly at z_{ref} , which suggests that PDF is too accurate. We do not expect to see such a feature in the presence of random uncertainties. While we have not fully understood the origin of the peak, we tentatively interpret it as a sign of over-fitting. Most likely, this peak is due to FRANKEN-Zs inclusion of both the training and target errors when deriving likelihoods. Unlike other nearest neighbor methods such as NNPZ which select neighbors and derive weights using Monte Carlo procedures based on (modifications to the) Euclidean norm, FRANKEN-Z computes the intrinsic likelihood expected if training/testing objects were Monte Carlo realizations of the same underlying galaxy (Speagle et al. in prep.). Objects whose photometry between the Wide-

depth stacks and Deep/UltraDeep observations are not fully independent can thus sometimes deviate much less than expected, leading to large contributions to the posterior and subsequent signs of over-fitting. We note that numerous cross-validation and hold-out tests have not found evidence of such behavior in the native training sample.

All of the codes have some degree of deviations from the flat PIT distribution. This motivates us to use the PIT distribution to empirically re-calibrate our $P(z)$ (Bordoloi et al. 2010) in our future releases as it will likely improve our overall performance.

We turn our attention to the other technique, CRPS. CRPS is a measure of a 'distance' between PDF and z_{ref} and is defined as

$$CRPS = \int_{-\infty}^{+\infty} \{PIT(z) - H(z - z_{ref})\}^2 dz, \quad (19)$$

where $H(z - z_{ref})$ the Heaviside step-function;

$$H(x) = \begin{cases} 0 & \text{if } x < 0 \\ 1 & \text{if } x \geq 0. \end{cases} \quad (20)$$

The right panels of Fig. 14 show CRPS for all the codes. When PDFs are calibrated well, the mean CRPS is small. A large CRPS is an indication of incorrect PDF. To the first order, all the codes perform similarly well; $\langle \log CRPS \rangle \sim -1$. However, there are small differences in CRPS between the codes and machine-learning codes once again tend to perform better than the classical template-fitting code.

It is interesting to note that a code with good performance with point estimates does not necessarily give a small CRPS. For instance, EPHOR_AB has a smaller loss than EPHOR as shown in Fig. 8. However, CRPS in Fig. 14 is larger, suggesting that PDF is less accurate. The PIT distribution indicates that EPHOR has over-dispersed PDFs, and this over-dispersed PDFs are likely driving the slightly larger CRPS. The analysis here suggests that accurate point estimates do not necessarily mean that PDFs are accurate. They are obviously closely related to each other but not exactly the same. Thus, in order to evaluate the photo- z performance, one needs to look both at the point estimates and PDFs.

7 Data Products

We make our photo- z products available to the community. This section summarizes our target selection criteria, 'common' outputs that are available for all the codes, as well as code-specific outputs.

HSC-SSP Public Data Release 1 (PDR1) includes our photo- z 's for the Deep and UltraDeep layers, covering over 30 square degrees in total. Due to a technical issue during the photo- z production run, we were unable to include our photo- z 's for the Wide layer in PDR1, but they were made public as part of the first incremental data release occurred in June 2017. It is

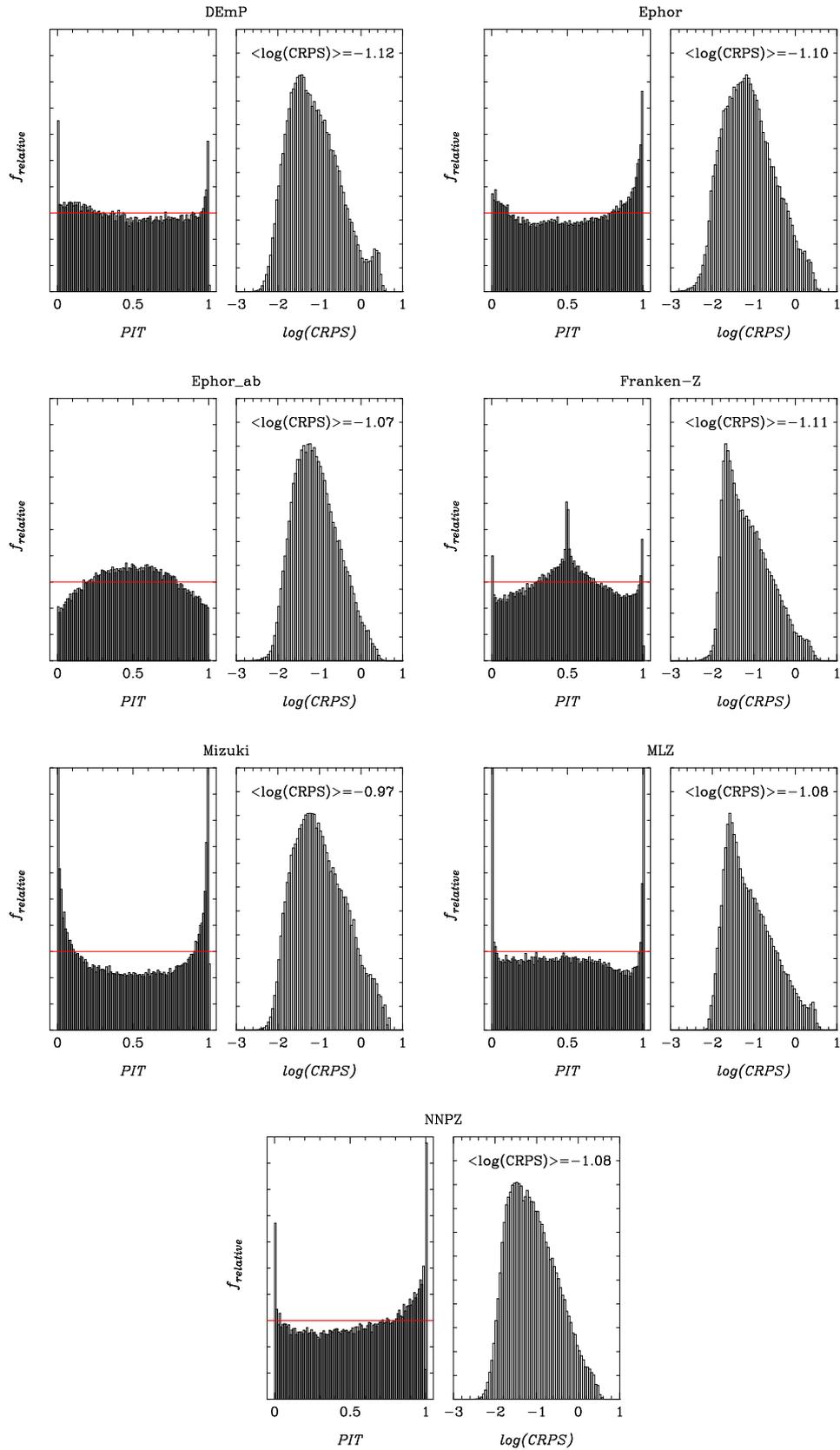


Fig. 14. PIT (left) and CRPS (right) for all the codes. The red horizontal line in the left panel is just to guide the eye.

important to note that each code applies various cuts to select objects for photo- z production. That is, each code is applied to a different set of objects (but with a significant overlap) due to features of the code. Table 5 summarizes the target selection by codes. The table also indicates whether there are additional outputs from the code, which we will elaborate below. Most codes imposed `detect_is_primary` to select primary objects, except for EPHOR. DEmP and MLZ compute photo- z 's for all the primary objects, but FRANKEN-Z and NNPZ requires good photometry in all the bands in addition to the primary flag. Mizuki computes photo- z 's for primary objects with good CModel photometry in at least 3 bands (inclusive).

All the codes generate a PDF for each object. We run a common script to compute various point estimates, confidence intervals and other useful statistics. The common outputs are summarized in Table 4. In addition to these common outputs, there are code-specific outputs as follows.

FRANKEN-Z

- `model_llmin`: $-2\ln(\max(\mathcal{L}_i)) = \min(\chi_n^2(i) - n(i))$, where $n(i) = 5$ is the number of bands used in the fit.
- `model_evidence`: $-2\ln(\text{evidence}) = 2\ln(\sum_i \mathcal{L}_i)$, where $\mathcal{L}_i = \exp\{-0.5[\chi_n^2(i) - n(i)]\}$ and the sum over i is taken over all unique neighbors.
- `model_ntype`: Number of unique neighbors used in the fit grouped by redshift type (spec, g/prism, and many-band photo- z).
- `model_ptype`: Fraction of normalized likelihood contributed by each redshift type.
- `model_nsurvey`: As above, but grouped by parent survey (SDSS, etc.).
- `model_psurvey`: As above, but contributed by by each parent survey.

Mizuki

- `reduced_chisq`, χ_ν^2 : Reduced chi-squares of the best-fit model. It is recommended to remove objects having $\chi_\nu^2 > 5$ for scientific use.
- `stellar_mass`: Median stellar mass derived from $P(M_*)$, which is stellar mass PDF marginalized over all the other parameters. The 68% confidence intervals are also available. All the uncertainties on physical parameters include uncertainties from photo- z 's.
- `sfr`: Median star formation rate with 68% intervals.
- `tauv`, τ_V : Median dust attenuation in the V-band with 68% intervals. Note that $A_V = 1.09\tau_V$.
- `prob_x`: x is either `gal`, `qso` or `star`, which denote the relative probability that an object is galaxy, QSO and star.
- `rest-frame magnitudes`: Rest-frame magnitudes in the GALEX, SDSS, HSC, and WFCAM filters. Only the magnitudes from the best-fit template at the median redshifts are computed and no uncertainties are currently available.

MLZ

- `flux_binary_flag`: Binary flag to show how many CModel fluxes at different filters are available,

$$f = \sum_{i=0}^4 \{2^{9-i} P F_i + 2^{4-i} N F_i\}, \quad (21)$$

where $P F_i = 1$ if $\text{flux}_i > \sigma \text{flux}_i$, and $N F_i = 1$ if $|\text{flux}_i| > \sigma \text{flux}_i$, and 0 otherwise. Index i denotes filters with 0 being g-band and 4 being y-band. If the object is well measured in all five bands, the flag have value 1023.

All of the catalog products such as photo- z point estimates are available in the database. The full PDFs are stored in the fits format and are available from the photo- z page of the PDR1 site.

8 Discussion and Summary

We have presented the photo- z 's computed with several independent codes using the data from HSC-SSP. We have constructed the training sample by combining spec- z , grism- z , and high accuracy photo- z and applied a weight to each object to reproduce the color-magnitude distribution of galaxies in the Wide layer. The codes are trained, validated, and tested using this training sample. We also use the COSMOS wide-depth stacks, in which the photometry is quasi-independent from the training sample, in order to evaluate the seeing and depth dependence of our photo- z performance.

We have compared the performance between the codes in Section 5. There are trends common to all the codes such as, (1) our photo- z 's are most accurate at $0.2 \lesssim z \lesssim 1.5$ where we can straddle the 4000Å break with our filter set, and (2) accuracy is nearly constant at $i \lesssim 23$ and becomes worse at fainter magnitudes. We use a few different algorithms in our machine-learning codes (i.e., neural network, nearest-neighbor, self-organizing map), but all the machine-learning codes perform better than the classical template fitting code (Mizuki). Although this may not be a firm, general conclusion because we have only one template-fitting code (and it was trained against an old version of the training sample with problematic weights), this may have implications for our future photo- z strategy.

It is not a surprising result that machine-learning outperforms the classical template-fitting. There are multiple reasons for this. One of them would be that template-fitting codes suffer directly from systematic effects in the photometry such as less accurate CModel photometry at bright magnitudes (see Aihara et al. 2017), while machine-learning codes make the empirical mapping between the photometry and redshift including such systematic effects. Machine-learning codes are thus less prone to systematic effects.

However, in order to train a machine-learning code, we need an unbiased training sample. This is a fundamentally difficult

problem because photometry always goes deeper than spectroscopy (at least with the current detector technology) and there is no complete spectroscopic sample down to faint enough (e.g., $i = 25$) magnitudes. There are on-going efforts to mitigate the problem and that will be useful for weak-lensing science, in which only relatively bright galaxies are used. However, in the UltraDeep layers of HSC-SSP for instance, we reach deeper than $i = 27$, where we have few spectroscopic redshifts.

While further spectroscopic efforts are definitely needed, another way to mitigate the problem would be to combine the template-fitting and machine-learning. We can first use the template-fitting technique with photometry in many filters. If our understanding of galaxy SEDs is reasonable, we can *assume* that these many-band photo- z 's are relatively accurate even beyond the depth of the spectroscopic limit. We can then train machine-learning codes against these many-band photo- z 's using much fewer filters to compute photo- z 's over a wide area.

In fact, this is exactly what we did in our photo- z training; we trained our 5-band photo- z 's against the COSMOS many-band photo- z catalog (Laigle et al. 2016). However, there are problems in the current dataset. First, the current optical data in COSMOS used in the photo- z calculation is not very deep, roughly 30-60 min integration, and it is not quite deep enough to train our codes for the Wide survey with 20 min integration. Fortunately, the UltraDeep COSMOS data from HSC-SSP is much deeper and that will solve this problem. Another problem is that COSMOS is currently the only wide enough field observed in many filters and high accuracy photo- z 's are available. As discussed in Section 6.1, there are significant large-scale structures even in COSMOS with multiple redshift peaks. We have re-weighted the training sample to reproduce the multi-color distribution of galaxies in the Wide layer and that largely reduces the effects of large-scale structures in COSMOS. But, it will still be very useful to have multiple COSMOS-like fields to suppress any field-specific systematics. UDS may be the next COSMOS field given its deep optical to IR data over the wide area, although intensive spectroscopic efforts are unfortunately missing in the field. There are also very narrow spikes in the $N(z)$ distribution of COSMOS, which are likely introduced by attractor solutions in the photo- z code and are not accounted for by the re-weighting. We need to run multiple template-fitting codes, not just one, to suppress such systematics.

We should also resort to clustering techniques to circumvent the problem. There are on-going efforts on clustering-based $N(z)$ estimations in HSC and we hope to report on that in our future paper. The technique does not suffer from any problems with photometry as it only requires positional information. A dense spectroscopic sample over the entire redshift range is needed, but SDSS already offers it at least for tests of $N(z)$ reconstruction in the Wide layer. We could also apply the technique to validate the many-band photo- z 's at very faint

magnitudes, where no spectroscopic data is available, to check how reliable many-band photo- z 's are beyond the reach of spectroscopic sensitivities. It is an open question how to handle the evolution of the galaxy bias, but the clustering-based redshift inference is certainly a promising way forward.

We have focused on redshifts in this paper, but there are other information we would need for science such as stellar mass and star formation rates of galaxies. A template-fitting code delivers such information, but we could also train machine-learning codes to compute these physical properties. The training sample will again come from COSMOS-like fields and we probably need to run multiple codes with templates from multiple stellar population synthesis codes in order to have a sense for systematics in the physical properties. That will also be our next step.

Aside from the problem of the training sample, there is another question of whether we should 'synthesize' photo- z estimates from all the codes into one, master photo- z . We probably should do so since the photo- z synthesis hopefully reduces uncertainties in each photo- z estimates under the assumption that not all the codes make the same mistake. It is also good for users to have just one photo- z for each object. Our preliminary analysis performed in an earlier photo- z production run suggests that, when there is a code that performs significantly better than the others, that code tends to dominate the master photo- z . However, in this release, most of the codes perform equally well and it is probably worth testing the photo- z synthesis again. This is another future task of the HSC photo- z group.

Finally, we remind the readers once again that the photo- z products discussed in this paper are publicly available. The photo- z point estimates, confidence and risk parameters, as well as other ancillary information are all stored in the database. A full $P(z)$ for each object is available in the fits format and can be downloaded from the photo- z page on the data release site. Some of our codes suffered from sub-optimal weights used in the training and also from over-training. We hope to mitigate these issues and release improved versions of our photo- z products in a future incremental release of HSC-SSP.

Acknowledgment

The Hyper Suprime-Cam (HSC) collaboration includes the astronomical communities of Japan and Taiwan, and Princeton University. The HSC instrumentation and software were developed by the National Astronomical Observatory of Japan (NAOJ), the Kavli Institute for the Physics and Mathematics of the Universe (Kavli IPMU), the University of Tokyo, the High Energy Accelerator Research Organization (KEK), the Academia Sinica Institute for Astronomy and Astrophysics in Taiwan (ASIAA), and Princeton University. Funding was

contributed by the FIRST program from Japanese Cabinet Office, the Ministry of Education, Culture, Sports, Science and Technology (MEXT), the Japan Society for the Promotion of Science (JSPS), Japan Science and Technology Agency (JST), the Toray Science Foundation, NAOJ, Kavli IPMU, KEK, ASIAA, and Princeton University.

This paper makes use of software developed for the Large Synoptic Survey Telescope. We thank the LSST Project for making their code available as free software at <http://dm.lsst.org>.

The Pan-STARRS1 Surveys (PS1) have been made possible through contributions of the Institute for Astronomy, the University of Hawaii, the Pan-STARRS Project Office, the Max-Planck Society and its participating institutes, the Max Planck Institute for Astronomy, Heidelberg and the Max Planck Institute for Extraterrestrial Physics, Garching, The Johns Hopkins University, Durham University, the University of Edinburgh, Queen's University Belfast, the Harvard-Smithsonian Center for Astrophysics, the Las Cumbres Observatory Global Telescope Network Incorporated, the National Central University of Taiwan, the Space Telescope Science Institute, the National Aeronautics and Space Administration under Grant No. NNX08AR22G issued through the Planetary Science Division of the NASA Science Mission Directorate, the National Science Foundation under Grant No. AST-1238877, the University of Maryland, and Eotvos Lorand University (ELTE) and the Los Alamos National Laboratory.

This paper is based on data collected at the Subaru Telescope and retrieved from the HSC data archive system, which is operated by Subaru Telescope and Astronomy Data Center at National Astronomical Observatory of Japan. We thank the COSMOS team for making their private spectroscopic redshift catalog available for our calibrations. MT acknowledges supported by JSPS KAKENHI Grant Number JP15K17617. AN is supported in part by MEXT KAKENHI Grant Number 16H01096. JSS is supported by the National Science Foundation Graduate Research Fellowship under Grant No. 2016222625. Any opinion, findings, and conclusions or recommendations expressed in this material are those of the authors(s) and do not necessarily reflect the views of the National Science Foundation. HM was supported by the U.S. DOE under Contract DE-AC02-05CH11231, and by the NSF under grants PHY-1316783 and PHY-1638509. HM was also supported by the JSPS Grant-in-Aid for Scientific Research (C) (No. 17K05409), Scientific Research on Innovative Areas (No. 15H05887), and by WPI, MEXT, Japan. We thank Jun Nakano for discussions on the training of machine-learning codes. We thank the anonymous referee for a very useful report, which helped improve the paper.

Appendix 1 Previous Internal Photo- z Releases

As summarized in Aihara et al. (2017), we have made 5 internal data releases. For each release, the HSC photo- z working group computed photo- z 's using several independent codes and released the photo- z products to the collaboration. As these internal photo- z products are used in our science papers, we briefly summarize them here.

This paper is based on our photo- z products in the S16A internal data release (i.e., latest release at the time of writing). In the current release, we have used 6 codes. But, we started with 4 codes (DEMP, MLZ, Mizuki, and LePhare) in the first data release (S14A0). FRANKEN-Z was included in S15B and EPHOR in S16A. For MLZ, random-forest was used to compute photo- z 's until S15B and it changed to SOM in S16A. In the early runs, we used a template-fitting code, LePhare, but it was later replaced with NNPZ, which performs better. There have been incremental updates in all the codes in each release, which helped steadily improve our photo- z performance over the years. But, the performance in the earlier runs is not drastically different from that presented in this paper. Thus, the accuracy quoted in this paper can be used as a rough reference to our previous releases. Once again, the photo- z 's for PDR1 are based on the S16A internal release.

Our calibration strategy in earlier releases were similar to the one presented in this paper, but we almost exclusively relied on the many-band photo- z 's from COSMOS. We cross-matched the HSC objects with the COSMOS photo- z catalog by position and split it into two: training+validation and test. Each photo- z runner used the first sample to train and validate the code and applied the trained code to the second sample to test the performance. While this approach worked well for faint objects, bright nearby objects were under-represented in COSMOS and we discovered problems with low- z objects in the Wide area. This led to the combined sample of bright spec- z sample and faint photo- z sample used in the training in this paper. Also, the best point estimator and the risk parameter were first introduced in S16A and in this paper and were not used in our previous releases. Most papers based on our previous photo- z products use z_{median} and $C(z_{median})$ instead.

Appendix 2 Biases and scatter in the physical parameter estimates by Mizuki

Mizuki infers physical properties of galaxies such as stellar mass and star formation rates (SFRs) self-consistently in addition to redshifts. This section evaluates how accurate the physical parameter estimates are. For this goal, we use data from the Newfirm Medium Band Survey (NMBS; Whitaker et al. 2011). We here focus on the AEGIS field and use the stellar mass and SFR estimates by Whitaker et al. (2011) based on the NMBS

and multi-wavelength data available in AEGIS.

Fig 15 compares stellar mass and SFR from Mizuki against NMBS. As shown in the main body of the paper, our photo- z 's are not very accurate at $z \gtrsim 1.5$, where we lose the 4000Å break, and we focus on galaxies at $z < 1.5$ here. Note that redshift is not fixed to those from NMBS but left as a free parameter. Overall, our stellar mass and SFR agree well with those from NMBS over the entire plotted range with a scatter of about 0.25 dex, including photo- z errors. However, there is a systematic bias; stellar mass is over-estimated by 0.2 dex and SFR underestimated by 0.1 dex. These biases in the physical properties are a function of redshift as shown in the top panels. The biases are likely due to combination of template error functions and physical priors applied (Tanaka 2015). Work is in progress to reduce the systematic biases, but we note that a level of 0.3 dex biases are relatively common in this field; van Dokkum et al. (2014) found a relatively large stellar mass offset of $0.2 \sim -0.3$ dex between 3D-HST and UltraVISTA catalogs even though both catalogs have deep photometry in many filters. Part of the bias we observe here might come from systematics in the data (either in HSC or NMBS).

References

- Abazajian, K., et al. 2003, AJ, 126, 2081
- Aihara, H., Armstrong, R., Bickerton, S., et al. 2017, arXiv:1702.08449
- Aihara, H., Arimoto, N., Armstrong, R., et al. 2017, arXiv:1704.05858
- Alam, S., et al. 2015, ApJS, 219, 12
- Arnouts, S., et al. 1999, MNRAS, 310, 540
- Beers, T. C., Flynn, K., & Gebhardt, K. 1990, AJ, 100, 32
- Benitez, N. 2000, ApJ, 536, 571
- Bordoloi, R., Lilly, S. J., & Amara, A. 2010, MNRAS, 406, 881
- L. Breiman, 2001, Machine Learning, 45, 1
- Bolzoniella, M., Miralles, J. -M., & Pelló, R., 2000, A&A, 363, 476
- Bonnett, C. et al. 2016, PhRvD, 94, 042005
- Bosch, J., Armstrong, R., Bickerton, S., et al. 2017, arXiv:1705.06766
- Bradshaw, E. J., Almaini, O., Hartley, W. G., et al. 2013, MNRAS, 433, 194
- Brammer, G. B., van Dokkum, P. G., Coppi, P. 2008 ApJ, 686, 1503
- Brammer, G. B., et al. 2012, ApJS, 200, 13
- Brescia, M. et al. 2016, PASP, 126, 783
- Bruzual, G., & Charlot, S. 2003, MNRAS, 344, 1000
- Calzetti, D., Armus, L., Bohlin, R. C., et al. 2000, ApJ, 533, 682
- S. Carliles, T Budavari, S. Heinis, C. Priebe, & A. Szalay, 2010, ApJ, 712, 511
- M. Carrasco Kind, & R. J. Brunner, 2013, MNRAS, 432, 1483
- Chabrier, G. 2003, PASP, 115, 763
- Cool, R. J., Moustakas, J., Blanton, M. R., et al. 2013, ApJ, 767, 118
- Coil, A. et al. 2011, ApJ, 743, 46
- Collister, A. & Lahav, O. 2004, PASP, 116, 345
- Cooper, M. C., et al. 2011, ApJS, 193, 14
- Cooper, M. C., et al. 2012, MNRAS, 419, 3018
- Coupon, J. et al. 2009, A&A, 500, 981
- Cunha, C. E., Lima, M., Oyaizu, H., Frieman, J., & Lin, H. 2009, MNRAS, 396, 2379
- Dahlen, T., et al. 2013, ApJ, 775, 93
- Davis, M., Faber, S. M., Newman, J., et al. 2003, Proc. SPIE, 4834, 161
- de Jong, J. T. A., Kuijken, K., Applegate, D., et al. 2013, the Messenger, 154, 44
- Drinkwater, M. J., Jurek, R. J., Blake, C., et al. 2010, MNRAS, 401, 1429
- Feldmann, R. et al. 2006, MNRAS, 372, 565
- Flaugher, B. 2005, International Journal of Modern Physics A, 20, 3121
- Garilli, B., et al. 2014, A&A, 562, 23
- Heymans, C. et al. 2013, MNRAS, 432, 2433
- Hildebrandt, H. et al. 2008, A&A, 480, 703
- Hildebrandt, H. et al. 2010, A&A, 523, 31
- Hildebrandt, H. et al. 2012, MNRAS, 421, 2355
- Hildebrandt, H. et al. 2017, MNRAS, 465, 1454
- Hsieh, B. C., Yee, H. K. C., Lin, H., & Gladders, M. D. 2005, ApJS, 158, 161
- Hsieh, B. C., & Yee, H. K. C. 2014, ApJ, 792, 102
- Huang, S., Leauthaud, A., Murata, R., et al. 2017, arXiv:1705.01599
- Ilbert, O. et al. 2006, A&A, 457, 841
- Inoue, A. K. 2011, MNRAS, 415, 2920
- Ivezić, Ž, et al. (2008) "LSST: from science drivers to reference design and anticipated data products" arXiv:0805.2366v4
- Kilbinger, M. et al. 2013, MNRAS, 430, 2200
- Kingma, D. P., & Ba, J. 2014, arXiv:1412.6980
- Kotulla, R. et al. 2009, Ap&SS, 324, 347
- Laigle, C., McCracken, H. J., Ilbert, O., et al. 2016, ApJS, 224, 24
- Laureijs, R., Amiaux, J., Arduini, S., et al. 2015, arXiv:1110.3193
- Le Fèvre, O., et al. 2004, A&A, 428, 1043
- Le Fèvre, O., et al. 2005, A&A, 439, 845
- Le Fèvre, O., Cassata, P., Cucciati, O., et al. 2013, A&A, 559, A14
- Leistedt, B., & Hogg, D. W. 2016, arXiv:1612.00847
- Lilly, S. J., Le Brun, V., Maier, C., et al. 2009, ApJS, 184, 218
- lima, M. et al. 2008, MNRAS, 390, 118
- Liske, J., et al. 2015, MNRAS, 452, 2087
- Masters, A. et al. 2015, ApJ, 813, 53
- McLure, R. J., Pearce, H. J., Dunlop, J. S., et al. 2013, MNRAS, 428, 1088
- Miyazaki, S. et al. 2012, SPIE, 8446E, 0Z
- Momcheva, I. G., et al. 2016, ApJS, 225, 27
- Newman, J. A., et al. 2013, ApJS, 208, 5
- Polletta, M., Tajer, M., Maraschi, L., et al. 2007, ApJ, 663, 81
- Polsterer, K. L., D'Isanto, A., & Gieseke, F. 2016, arXiv:1608.08016
- Salvato, M., Hasinger, G., Ilbert, O., et al. 2009, ApJ, 690, 1250
- Skelton, R. E., et al. 2014, ApJS, 214, 24
- Singal, J. et al. 2011, PASP, 123, 615
- Silverman, J. D., Kashino, D., Sanders, D., et al. 2015, ApJS, 220, 12
- Tagliaferri, R., Longo, G., Andreon, S., et al. 2003, Lecture Notes in Computer Science, 2859, 226
- Tanaka, M. 2015, ApJ, 801, 20
- Tasca, L. A. M., et al. 2016, arXiv:1602.01842
- van Dokkum, P. G., Bezanson, R., van der Wel, A., et al. 2014, ApJ, 791, 45
- Walcher, J. et al. 2011, Ap&SS, 331, 1
- Westera, P., Lejeune, T., Buser, R., Cuisinier, F., & Bruzual, G. 2002, A&A, 381, 524
- Whitaker, K. E., Labbé, I., van Dokkum, P. G., et al. 2011, ApJ, 735, 86
- Wolf, C. et al. 2009, MNRAS, 397, 520

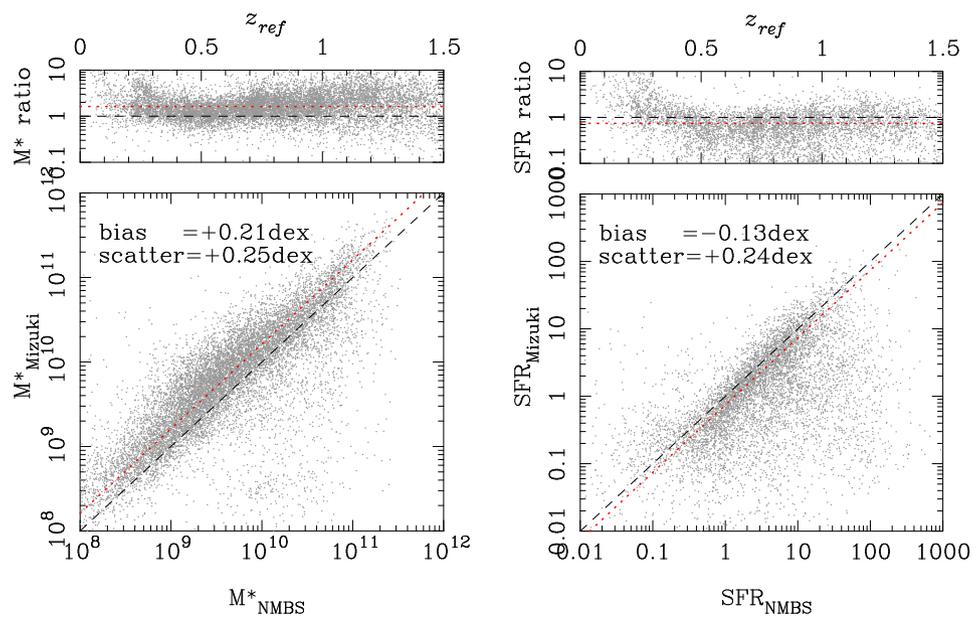


Fig. 15. Stellar mass (left) and SFR (right) from Mizuki plotted against those from NMBS. The top panel in each plot shows the ratio between Mizuki and NMBS as a function of redshift. The dashed lines show the perfect correspondence and the dotted lines show the mean bias.

Table 2. Photo- z statistics for all the codes as a function of magnitude. The number are for all galaxies down to $i = 25$.

Code	mag.	bias	σ_{conv}	$f_{outlier.conv}$	σ	$f_{outlier}$	$\langle L(\Delta z) \rangle$	
DEmP	18.50 – 18.75	–0.000	0.060	0.430	0.023	0.463	0.373	
	18.75 – 19.00	+0.003	0.026	0.124	0.025	0.210	0.124	
	19.00 – 19.25	–0.001	0.015	0.000	0.017	0.145	0.027	
	19.25 – 19.50	+0.002	0.024	0.050	0.021	0.156	0.070	
	19.50 – 19.75	+0.001	0.025	0.090	0.023	0.209	0.101	
	19.75 – 20.00	+0.004	0.022	0.108	0.020	0.245	0.112	
	20.00 – 20.25	+0.004	0.024	0.047	0.023	0.191	0.079	
	20.25 – 20.50	+0.004	0.021	0.039	0.019	0.178	0.061	
	20.50 – 20.75	+0.007	0.023	0.052	0.021	0.186	0.077	
	20.75 – 21.00	+0.005	0.021	0.037	0.020	0.166	0.058	
	21.00 – 21.25	+0.006	0.024	0.045	0.022	0.171	0.072	
	21.25 – 21.50	+0.005	0.022	0.037	0.021	0.182	0.066	
	21.50 – 21.75	+0.006	0.023	0.040	0.021	0.156	0.064	
	21.75 – 22.00	+0.005	0.024	0.044	0.024	0.165	0.073	
	22.00 – 22.25	+0.005	0.024	0.042	0.023	0.163	0.072	
	22.25 – 22.50	+0.004	0.025	0.049	0.024	0.166	0.078	
	22.50 – 22.75	+0.003	0.028	0.044	0.027	0.153	0.078	
	22.75 – 23.00	+0.001	0.030	0.045	0.030	0.150	0.082	
	23.00 – 23.25	+0.002	0.033	0.063	0.033	0.160	0.103	
	23.25 – 23.50	+0.000	0.039	0.089	0.038	0.173	0.128	
	23.50 – 23.75	–0.001	0.046	0.123	0.044	0.201	0.164	
	23.75 – 24.00	–0.001	0.057	0.167	0.054	0.217	0.208	
	24.00 – 24.25	–0.004	0.072	0.209	0.070	0.222	0.251	
	24.25 – 24.50	–0.007	0.090	0.261	0.089	0.227	0.297	
	24.50 – 24.75	–0.011	0.107	0.308	0.110	0.222	0.335	
	24.75 – 25.00	–0.014	0.121	0.331	0.127	0.208	0.357	
	EPHOR	18.50 – 18.75	–0.003	0.047	0.430	0.020	0.437	0.422
		18.75 – 19.00	+0.007	0.028	0.124	0.017	0.271	0.139
19.00 – 19.25		–0.000	0.016	0.023	0.018	0.133	0.037	
19.25 – 19.50		–0.004	0.023	0.040	0.024	0.201	0.077	
19.50 – 19.75		–0.000	0.024	0.087	0.021	0.176	0.092	
19.75 – 20.00		–0.002	0.026	0.073	0.024	0.191	0.099	
20.00 – 20.25		+0.002	0.021	0.044	0.022	0.205	0.078	
20.25 – 20.50		+0.001	0.021	0.052	0.020	0.164	0.071	
20.50 – 20.75		+0.003	0.023	0.047	0.023	0.157	0.069	
20.75 – 21.00		+0.002	0.022	0.040	0.021	0.157	0.065	
21.00 – 21.25		+0.002	0.023	0.048	0.023	0.157	0.071	
21.25 – 21.50		+0.001	0.023	0.037	0.024	0.144	0.064	
21.50 – 21.75		+0.001	0.024	0.042	0.024	0.145	0.066	
21.75 – 22.00		–0.000	0.025	0.053	0.026	0.165	0.078	
22.00 – 22.25		–0.000	0.025	0.048	0.025	0.168	0.079	
22.25 – 22.50		–0.001	0.026	0.056	0.026	0.172	0.084	
22.50 – 22.75		–0.001	0.029	0.049	0.029	0.153	0.083	
22.75 – 23.00		–0.002	0.031	0.056	0.031	0.159	0.092	
23.00 – 23.25		–0.001	0.035	0.071	0.034	0.164	0.109	
23.25 – 23.50		–0.003	0.040	0.101	0.037	0.183	0.137	
23.50 – 23.75		–0.003	0.047	0.137	0.044	0.211	0.175	
23.75 – 24.00		–0.004	0.057	0.184	0.052	0.235	0.217	
24.00 – 24.25		–0.006	0.071	0.224	0.066	0.243	0.259	
24.25 – 24.50		–0.011	0.087	0.259	0.085	0.235	0.293	
24.50 – 24.75		–0.017	0.104	0.312	0.110	0.226	0.333	
24.75 – 25.00		–0.024	0.119	0.335	0.125	0.210	0.356	
EPHOR_AB		18.50 – 18.75	–0.000	0.005	0.000	0.008	0.325	0.014
		18.75 – 19.00	–0.002	0.026	0.124	0.026	0.192	0.140
	19.00 – 19.25	–0.005	0.017	0.000	0.019	0.123	0.035	
	19.25 – 19.50	–0.004	0.026	0.021	0.021	0.105	0.046	
	19.50 – 19.75	–0.004	0.028	0.098	0.023	0.169	0.100	
	19.75 – 20.00	–0.003	0.025	0.110	0.021	0.229	0.121	
	20.00 – 20.25	–0.001	0.024	0.053	0.026	0.174	0.082	
	20.25 – 20.50	–0.001	0.023	0.038	0.021	0.147	0.061	
	20.50 – 20.75	+0.002	0.025	0.053	0.022	0.163	0.076	
	20.75 – 21.00	+0.001	0.022	0.042	0.022	0.143	0.059	
	21.00 – 21.25	+0.001	0.023	0.059	0.022	0.178	0.080	
	21.25 – 21.50	+0.001	0.023	0.050	0.022	0.169	0.072	
	21.50 – 21.75	+0.001	0.023	0.047	0.022	0.153	0.066	
	21.75 – 22.00	+0.000	0.023	0.050	0.024	0.165	0.075	
	22.00 – 22.25	–0.000	0.025	0.052	0.024	0.157	0.078	
	22.25 – 22.50	–0.001	0.026	0.053	0.025	0.162	0.078	
	22.50 – 22.75	–0.002	0.028	0.051	0.027	0.147	0.080	
	22.75 – 23.00	–0.003	0.030	0.052	0.030	0.148	0.085	
	23.00 – 23.25	–0.003	0.033	0.069	0.032	0.155	0.102	
	23.25 – 23.50	–0.004	0.039	0.086	0.037	0.164	0.123	
	23.50 – 23.75	–0.005	0.047	0.113	0.044	0.182	0.155	
	23.75 – 24.00	–0.005	0.057	0.151	0.052	0.200	0.194	
	24.00 – 24.25	–0.005	0.069	0.194	0.068	0.209	0.237	
	24.25 – 24.50	–0.006	0.081	0.222	0.081	0.206	0.264	
	24.50 – 24.75	–0.007	0.095	0.263	0.097	0.215	0.303	
	24.75 – 25.00	–0.009	0.104	0.292	0.110	0.212	0.326	
	18.75 – 19.00	–0.000	0.021	0.000	0.028	0.120	0.039	
	19.00 – 19.25	–0.005	0.012	0.000	0.010	0.228	0.032	

Table 2. (Continued)

	19.25 – 19.50	–0.001	0.013	0.011	0.015	0.189	0.036
	19.50 – 19.75	–0.002	0.012	0.018	0.015	0.182	0.038
	19.75 – 20.00	–0.001	0.015	0.015	0.017	0.145	0.043
	20.00 – 20.25	–0.001	0.012	0.019	0.013	0.199	0.039
	20.25 – 20.50	–0.002	0.013	0.024	0.014	0.200	0.043
	20.50 – 20.75	–0.001	0.012	0.029	0.013	0.195	0.045
	20.75 – 21.00	–0.002	0.013	0.022	0.014	0.162	0.038
	21.00 – 21.25	–0.001	0.015	0.025	0.016	0.156	0.046
	21.25 – 21.50	–0.001	0.014	0.033	0.015	0.178	0.046
	21.50 – 21.75	–0.001	0.015	0.030	0.016	0.173	0.048
Franken-Z	21.75 – 22.00	–0.001	0.019	0.042	0.019	0.173	0.060
	22.00 – 22.25	–0.001	0.019	0.039	0.020	0.174	0.062
	22.25 – 22.50	–0.001	0.022	0.047	0.022	0.173	0.069
	22.50 – 22.75	–0.002	0.024	0.043	0.025	0.152	0.069
	22.75 – 23.00	–0.003	0.027	0.046	0.027	0.158	0.079
	23.00 – 23.25	–0.003	0.032	0.067	0.031	0.172	0.103
	23.25 – 23.50	–0.003	0.035	0.088	0.034	0.180	0.122
	23.50 – 23.75	–0.003	0.043	0.113	0.041	0.197	0.154
	23.75 – 24.00	–0.003	0.054	0.153	0.050	0.214	0.195
	24.00 – 24.25	–0.004	0.067	0.197	0.064	0.224	0.239
	24.25 – 24.50	–0.007	0.080	0.234	0.079	0.223	0.273
	24.50 – 24.75	–0.009	0.096	0.279	0.096	0.226	0.310
	24.75 – 25.00	–0.009	0.106	0.303	0.112	0.217	0.332
	18.50 – 18.75	–0.006	0.131	0.430	0.051	0.464	0.481
	18.75 – 19.00	+0.000	0.032	0.124	0.036	0.278	0.190
	19.00 – 19.25	–0.009	0.028	0.015	0.036	0.115	0.075
	19.25 – 19.50	–0.004	0.035	0.066	0.036	0.161	0.112
	19.50 – 19.75	+0.001	0.043	0.130	0.037	0.228	0.178
	19.75 – 20.00	+0.006	0.041	0.132	0.041	0.237	0.185
	20.00 – 20.25	+0.006	0.038	0.127	0.040	0.234	0.171
	20.25 – 20.50	+0.004	0.033	0.086	0.030	0.210	0.122
	20.50 – 20.75	+0.006	0.035	0.097	0.032	0.218	0.126
	20.75 – 21.00	+0.003	0.032	0.078	0.033	0.179	0.110
	21.00 – 21.25	+0.001	0.035	0.094	0.034	0.174	0.127
	21.25 – 21.50	–0.001	0.032	0.107	0.029	0.208	0.134
Mizuki	21.50 – 21.75	+0.001	0.033	0.095	0.030	0.166	0.121
	21.75 – 22.00	–0.001	0.036	0.100	0.033	0.184	0.132
	22.00 – 22.25	–0.001	0.035	0.095	0.032	0.187	0.126
	22.25 – 22.50	–0.001	0.036	0.099	0.034	0.184	0.131
	22.50 – 22.75	–0.002	0.036	0.085	0.035	0.172	0.123
	22.75 – 23.00	–0.002	0.041	0.093	0.039	0.171	0.136
	23.00 – 23.25	+0.001	0.045	0.103	0.042	0.174	0.146
	23.25 – 23.50	–0.000	0.051	0.126	0.048	0.186	0.170
	23.50 – 23.75	–0.001	0.059	0.149	0.058	0.192	0.197
	23.75 – 24.00	–0.002	0.071	0.198	0.070	0.212	0.244
	24.00 – 24.25	–0.006	0.086	0.246	0.086	0.217	0.286
	24.25 – 24.50	–0.008	0.103	0.275	0.102	0.212	0.316
	24.50 – 24.75	–0.008	0.124	0.334	0.121	0.228	0.364
	24.75 – 25.00	–0.011	0.141	0.362	0.137	0.222	0.391
	18.50 – 18.75	+0.014	0.087	0.430	0.424	0.000	0.435
	18.75 – 19.00	–0.002	0.051	0.062	0.050	0.078	0.132
	19.00 – 19.25	–0.002	0.038	0.008	0.046	0.062	0.076
	19.25 – 19.50	–0.001	0.051	0.044	0.046	0.091	0.107
	19.50 – 19.75	+0.006	0.054	0.090	0.049	0.154	0.153
	19.75 – 20.00	+0.013	0.055	0.109	0.053	0.164	0.170
	20.00 – 20.25	+0.012	0.052	0.065	0.056	0.127	0.142
	20.25 – 20.50	+0.004	0.042	0.051	0.045	0.138	0.111
	20.50 – 20.75	+0.008	0.045	0.091	0.041	0.159	0.125
	20.75 – 21.00	+0.006	0.039	0.069	0.043	0.151	0.116
	21.00 – 21.25	+0.006	0.039	0.068	0.041	0.146	0.116
	21.25 – 21.50	+0.005	0.038	0.074	0.037	0.170	0.111
MLZ	21.50 – 21.75	+0.006	0.039	0.069	0.037	0.135	0.106
	21.75 – 22.00	+0.004	0.039	0.073	0.037	0.155	0.112
	22.00 – 22.25	+0.002	0.038	0.075	0.038	0.163	0.115
	22.25 – 22.50	+0.000	0.039	0.066	0.039	0.147	0.109
	22.50 – 22.75	–0.001	0.038	0.067	0.039	0.143	0.110
	22.75 – 23.00	–0.004	0.040	0.067	0.040	0.148	0.112
	23.00 – 23.25	–0.002	0.043	0.088	0.042	0.163	0.130
	23.25 – 23.50	–0.003	0.046	0.106	0.044	0.175	0.148
	23.50 – 23.75	–0.004	0.054	0.138	0.052	0.194	0.183
	23.75 – 24.00	–0.005	0.065	0.184	0.062	0.214	0.225
	24.00 – 24.25	–0.005	0.077	0.230	0.075	0.229	0.265
	24.25 – 24.50	–0.007	0.092	0.274	0.095	0.229	0.306
	24.50 – 24.75	–0.009	0.107	0.317	0.110	0.234	0.341
	24.75 – 25.00	–0.012	0.119	0.343	0.126	0.228	0.364
	18.50 – 18.75	+0.004	0.007	0.000	0.009	0.379	0.020
	18.75 – 19.00	–0.001	0.034	0.000	0.031	0.079	0.055
	19.00 – 19.25	–0.001	0.027	0.008	0.032	0.094	0.059
	19.25 – 19.50	–0.005	0.039	0.010	0.039	0.079	0.070
	19.50 – 19.75	+0.001	0.028	0.040	0.029	0.127	0.073
	19.75 – 20.00	+0.002	0.031	0.048	0.031	0.150	0.084

Table 2. (Continued)

	20.00 – 20.25	+0.004	0.032	0.046	0.034	0.144	0.094
	20.25 – 20.50	+0.000	0.027	0.042	0.027	0.164	0.075
	20.50 – 20.75	+0.001	0.031	0.059	0.030	0.166	0.089
	20.75 – 21.00	–0.000	0.027	0.048	0.027	0.161	0.078
	21.00 – 21.25	–0.000	0.027	0.051	0.027	0.162	0.081
	21.25 – 21.50	–0.000	0.027	0.046	0.028	0.148	0.072
NNPZ	21.50 – 21.75	–0.000	0.027	0.039	0.026	0.149	0.071
	21.75 – 22.00	–0.001	0.028	0.051	0.028	0.153	0.083
	22.00 – 22.25	–0.001	0.029	0.056	0.028	0.163	0.088
	22.25 – 22.50	–0.001	0.030	0.061	0.030	0.161	0.092
	22.50 – 22.75	–0.001	0.032	0.056	0.031	0.148	0.091
	22.75 – 23.00	–0.002	0.035	0.061	0.035	0.151	0.101
	23.00 – 23.25	–0.002	0.038	0.076	0.038	0.164	0.119
	23.25 – 23.50	–0.003	0.042	0.106	0.040	0.187	0.145
	23.50 – 23.75	–0.003	0.050	0.138	0.048	0.208	0.178
	23.75 – 24.00	–0.004	0.061	0.185	0.057	0.227	0.220
	24.00 – 24.25	–0.007	0.074	0.231	0.071	0.239	0.264
	24.25 – 24.50	–0.011	0.089	0.275	0.090	0.239	0.303
	24.50 – 24.75	–0.015	0.104	0.319	0.112	0.225	0.337
	24.75 – 25.00	–0.017	0.115	0.333	0.122	0.219	0.354

Table 3. Photo- z statistics for all the codes as a function of z_{phot} . The number are for all galaxies down to $i = 25$.

Code	z_{phot}	bias	σ_{conv}	$f_{outlier,conv}$	σ	$f_{outlier}$	$< L(\Delta z) >$
DEmP	0.00 – 0.10	+0.014	0.049	0.213	0.031	0.260	0.221
	0.10 – 0.20	+0.004	0.044	0.112	0.042	0.168	0.157
	0.20 – 0.30	+0.004	0.049	0.192	0.046	0.269	0.219
	0.30 – 0.40	+0.002	0.042	0.135	0.042	0.238	0.181
	0.40 – 0.50	+0.003	0.057	0.170	0.053	0.220	0.213
	0.50 – 0.60	+0.007	0.055	0.200	0.047	0.256	0.231
	0.60 – 0.70	+0.004	0.037	0.132	0.033	0.228	0.163
	0.70 – 0.80	+0.003	0.041	0.115	0.042	0.210	0.154
	0.80 – 0.90	-0.006	0.047	0.100	0.049	0.171	0.149
	0.90 – 1.00	-0.000	0.040	0.148	0.038	0.239	0.165
	1.00 – 1.10	-0.009	0.067	0.213	0.090	0.162	0.225
	1.10 – 1.20	-0.006	0.050	0.141	0.052	0.203	0.171
	1.20 – 1.30	-0.001	0.054	0.115	0.055	0.164	0.160
	1.30 – 1.40	-0.001	0.056	0.123	0.061	0.163	0.172
	1.40 – 1.50	-0.006	0.057	0.202	0.062	0.239	0.218
	1.50 – 1.60	-0.007	0.070	0.268	0.091	0.231	0.268
	1.60 – 1.70	-0.010	0.106	0.301	0.142	0.115	0.316
	1.70 – 1.80	+0.000	0.113	0.273	0.132	0.136	0.319
	1.80 – 1.90	+0.011	0.138	0.291	0.140	0.119	0.345
	1.90 – 2.00	+0.003	0.124	0.280	0.118	0.117	0.323
	2.00 – 2.10	+0.017	0.143	0.308	0.130	0.134	0.357
	2.10 – 2.20	+0.014	0.154	0.330	0.139	0.119	0.373
	2.20 – 2.30	+0.019	0.149	0.342	0.141	0.141	0.380
	2.30 – 2.40	+0.020	0.153	0.337	0.140	0.166	0.387
	2.40 – 2.50	+0.021	0.149	0.370	0.150	0.186	0.402
	2.50 – 2.60	+0.014	0.132	0.342	0.122	0.250	0.388
	2.60 – 2.70	-0.002	0.130	0.356	0.101	0.314	0.407
	2.70 – 2.80	+0.007	0.120	0.334	0.086	0.307	0.382
	2.80 – 2.90	+0.001	0.108	0.327	0.073	0.328	0.386
	2.90 – 3.00	-0.001	0.109	0.364	0.067	0.373	0.406
	3.00 – 3.10	+0.004	0.114	0.374	0.065	0.382	0.430
	3.10 – 3.20	-0.005	0.129	0.434	0.059	0.460	0.482
	3.20 – 3.30	-0.002	0.135	0.442	0.059	0.464	0.483
	3.30 – 3.40	-0.008	0.117	0.406	0.051	0.435	0.450
	3.40 – 3.50	-0.006	0.094	0.337	0.053	0.372	0.391
	3.50 – 3.60	+0.002	0.070	0.312	0.044	0.361	0.353
3.60 – 3.70	-0.002	0.073	0.305	0.046	0.331	0.356	
3.70 – 3.80	+0.007	0.086	0.321	0.052	0.337	0.374	
3.80 – 3.90	+0.016	0.101	0.344	0.057	0.357	0.401	
3.90 – 4.00	+0.024	0.099	0.313	0.058	0.322	0.377	
EPHOR	0.00 – 0.10	-0.045	0.092	0.408	0.338	0.003	0.420
	0.10 – 0.20	+0.002	0.054	0.155	0.048	0.202	0.207
	0.20 – 0.30	+0.002	0.052	0.190	0.049	0.268	0.219
	0.30 – 0.40	-0.003	0.042	0.152	0.039	0.253	0.194
	0.40 – 0.50	-0.000	0.052	0.181	0.046	0.248	0.216
	0.50 – 0.60	+0.005	0.065	0.251	0.050	0.296	0.274
	0.60 – 0.70	+0.000	0.040	0.161	0.034	0.254	0.188
	0.70 – 0.80	-0.004	0.046	0.157	0.044	0.237	0.188
	0.80 – 0.90	-0.012	0.047	0.101	0.046	0.176	0.149
	0.90 – 1.00	-0.003	0.045	0.182	0.040	0.262	0.190
	1.00 – 1.10	-0.017	0.064	0.215	0.090	0.159	0.223
	1.10 – 1.20	-0.016	0.053	0.147	0.052	0.192	0.178
	1.20 – 1.30	-0.006	0.049	0.083	0.048	0.139	0.132
	1.30 – 1.40	-0.002	0.049	0.094	0.051	0.155	0.143
	1.40 – 1.50	-0.004	0.052	0.172	0.051	0.237	0.193
	1.50 – 1.60	-0.000	0.065	0.262	0.067	0.280	0.262
	1.60 – 1.70	-0.007	0.109	0.316	0.152	0.111	0.327
	1.70 – 1.80	-0.009	0.127	0.313	0.147	0.114	0.341
	1.80 – 1.90	+0.002	0.119	0.249	0.122	0.112	0.304
	1.90 – 2.00	+0.002	0.133	0.274	0.124	0.098	0.322
	2.00 – 2.10	+0.035	0.142	0.294	0.133	0.100	0.344
	2.10 – 2.20	+0.032	0.137	0.343	0.140	0.110	0.354
	2.20 – 2.30	+0.034	0.155	0.338	0.148	0.120	0.385
	2.30 – 2.40	+0.007	0.134	0.312	0.128	0.204	0.368
	2.40 – 2.50	+0.021	0.142	0.349	0.138	0.201	0.388
	2.50 – 2.60	+0.033	0.132	0.370	0.143	0.212	0.389
	2.60 – 2.70	+0.039	0.121	0.338	0.127	0.221	0.377
	2.70 – 2.80	+0.020	0.118	0.275	0.092	0.221	0.344
	2.80 – 2.90	+0.010	0.095	0.281	0.076	0.270	0.343
	2.90 – 3.00	+0.007	0.090	0.312	0.069	0.315	0.353
	3.00 – 3.10	+0.011	0.126	0.368	0.080	0.354	0.423
	3.10 – 3.20	+0.004	0.113	0.364	0.070	0.370	0.419
	3.20 – 3.30	+0.005	0.125	0.406	0.069	0.409	0.453
	3.30 – 3.40	-0.001	0.104	0.354	0.062	0.379	0.412
	3.40 – 3.50	+0.004	0.099	0.364	0.054	0.405	0.410
	3.50 – 3.60	+0.007	0.062	0.262	0.042	0.316	0.304
3.60 – 3.70	+0.004	0.072	0.204	0.053	0.230	0.276	
3.70 – 3.80	+0.000	0.081	0.281	0.057	0.299	0.340	
3.80 – 3.90	+0.016	0.091	0.274	0.058	0.289	0.342	
3.90 – 4.00	-0.016	0.087	0.380	0.039	0.441	0.419	

Table 3. (Continued)

	0.00 – 0.10	+0.001	0.068	0.218	0.054	0.248	0.254
	0.10 – 0.20	–0.005	0.044	0.125	0.040	0.185	0.168
	0.20 – 0.30	–0.004	0.051	0.190	0.048	0.266	0.221
	0.30 – 0.40	–0.002	0.034	0.106	0.032	0.206	0.140
	0.40 – 0.50	+0.004	0.058	0.187	0.052	0.232	0.226
	0.50 – 0.60	+0.001	0.057	0.198	0.048	0.254	0.229
	0.60 – 0.70	–0.003	0.036	0.105	0.033	0.202	0.139
	0.70 – 0.80	+0.001	0.038	0.076	0.041	0.166	0.124
	0.80 – 0.90	–0.005	0.045	0.080	0.044	0.152	0.129
	0.90 – 1.00	–0.003	0.043	0.144	0.041	0.225	0.166
	1.00 – 1.10	–0.019	0.075	0.237	0.106	0.108	0.242
	1.10 – 1.20	–0.006	0.051	0.135	0.053	0.194	0.167
EPHOR_AB	1.20 – 1.30	–0.004	0.055	0.101	0.053	0.146	0.149
	1.30 – 1.40	–0.007	0.056	0.115	0.058	0.159	0.164
	1.40 – 1.50	–0.012	0.057	0.190	0.054	0.255	0.209
	1.50 – 1.60	–0.005	0.064	0.225	0.078	0.214	0.236
	1.60 – 1.70	–0.010	0.098	0.266	0.128	0.132	0.288
	1.70 – 1.80	–0.013	0.111	0.250	0.126	0.104	0.297
	1.80 – 1.90	–0.011	0.118	0.232	0.118	0.091	0.293
	1.90 – 2.00	–0.009	0.118	0.250	0.112	0.092	0.296
	2.00 – 2.10	–0.011	0.118	0.211	0.110	0.068	0.281
	2.10 – 2.20	–0.005	0.114	0.208	0.106	0.095	0.282
	2.20 – 2.30	+0.002	0.129	0.256	0.124	0.119	0.319
	2.30 – 2.40	+0.008	0.124	0.270	0.134	0.110	0.329
	2.40 – 2.50	+0.014	0.124	0.290	0.134	0.176	0.348
	2.50 – 2.60	–0.013	0.113	0.279	0.099	0.252	0.344
	2.60 – 2.70	–0.003	0.114	0.308	0.088	0.287	0.370
	2.70 – 2.80	–0.006	0.111	0.329	0.072	0.336	0.384
	2.80 – 2.90	–0.009	0.111	0.363	0.067	0.390	0.414
	2.90 – 3.00	–0.010	0.109	0.369	0.064	0.383	0.416
	3.00 – 3.10	–0.007	0.103	0.359	0.058	0.384	0.418
	3.10 – 3.20	–0.001	0.109	0.405	0.057	0.431	0.448
	3.20 – 3.30	–0.008	0.100	0.351	0.058	0.385	0.406
	3.30 – 3.40	–0.005	0.078	0.312	0.050	0.360	0.364
	3.40 – 3.50	–0.003	0.066	0.274	0.046	0.308	0.322
	3.50 – 3.60	–0.005	0.057	0.230	0.043	0.280	0.278
	3.60 – 3.70	–0.010	0.074	0.232	0.050	0.255	0.293
	3.70 – 3.80	–0.003	0.080	0.291	0.053	0.318	0.339
	3.80 – 3.90	–0.005	0.095	0.303	0.058	0.320	0.368
	3.90 – 4.00	–0.008	0.080	0.209	0.054	0.215	0.283
	0.00 – 0.10	+0.011	0.044	0.281	0.021	0.402	0.282
	0.10 – 0.20	–0.006	0.045	0.144	0.039	0.207	0.182
	0.20 – 0.30	–0.003	0.044	0.198	0.036	0.303	0.225
	0.30 – 0.40	–0.002	0.035	0.119	0.033	0.233	0.157
	0.40 – 0.50	–0.001	0.053	0.162	0.048	0.230	0.204
	0.50 – 0.60	+0.002	0.052	0.193	0.045	0.261	0.223
	0.60 – 0.70	–0.001	0.036	0.125	0.033	0.225	0.156
	0.70 – 0.80	–0.002	0.039	0.101	0.040	0.196	0.140
	0.80 – 0.90	–0.008	0.044	0.086	0.044	0.169	0.135
	0.90 – 1.00	–0.002	0.040	0.147	0.037	0.236	0.162
	1.00 – 1.10	–0.008	0.060	0.198	0.074	0.195	0.211
	1.10 – 1.20	–0.007	0.045	0.119	0.045	0.198	0.153
Franken-Z	1.20 – 1.30	–0.003	0.049	0.091	0.049	0.151	0.139
	1.30 – 1.40	–0.004	0.050	0.109	0.052	0.175	0.153
	1.40 – 1.50	–0.006	0.051	0.191	0.050	0.262	0.206
	1.50 – 1.60	–0.005	0.062	0.245	0.062	0.275	0.251
	1.60 – 1.70	–0.012	0.095	0.268	0.122	0.145	0.288
	1.70 – 1.80	+0.008	0.105	0.237	0.120	0.139	0.295
	1.80 – 1.90	+0.000	0.116	0.249	0.122	0.116	0.302
	1.90 – 2.00	–0.005	0.117	0.257	0.117	0.101	0.301
	2.00 – 2.10	+0.002	0.130	0.276	0.120	0.115	0.321
	2.10 – 2.20	+0.014	0.129	0.278	0.121	0.115	0.329
	2.20 – 2.30	+0.018	0.147	0.291	0.138	0.119	0.353
	2.30 – 2.40	+0.024	0.147	0.326	0.146	0.144	0.378
	2.40 – 2.50	+0.019	0.121	0.334	0.132	0.203	0.356
	2.50 – 2.60	+0.016	0.128	0.332	0.132	0.239	0.380
	2.60 – 2.70	+0.005	0.111	0.297	0.093	0.270	0.354
	2.70 – 2.80	–0.001	0.098	0.310	0.075	0.310	0.356
	2.80 – 2.90	+0.001	0.105	0.328	0.070	0.338	0.377
	2.90 – 3.00	+0.007	0.105	0.324	0.072	0.324	0.378
	3.00 – 3.10	+0.004	0.096	0.340	0.059	0.354	0.393
	3.10 – 3.20	+0.007	0.098	0.364	0.055	0.384	0.413
	3.20 – 3.30	+0.006	0.116	0.421	0.053	0.444	0.465
	3.30 – 3.40	+0.001	0.092	0.387	0.047	0.430	0.421
	3.40 – 3.50	–0.001	0.078	0.299	0.049	0.348	0.350
	3.50 – 3.60	+0.004	0.064	0.277	0.042	0.324	0.319
	3.60 – 3.70	+0.007	0.065	0.237	0.046	0.273	0.293
	3.70 – 3.80	+0.003	0.079	0.272	0.052	0.295	0.323
	3.80 – 3.90	+0.013	0.092	0.334	0.050	0.344	0.376
	3.90 – 4.00	+0.010	0.084	0.294	0.054	0.313	0.348
	0.00 – 0.10	–0.272	0.286	0.550	0.330	0.000	0.522

Table 3. (Continued)

	0.10 – 0.20	+0.001	0.070	0.283	0.048	0.317	0.301
	0.20 – 0.30	+0.007	0.059	0.193	0.055	0.257	0.231
	0.30 – 0.40	+0.005	0.042	0.132	0.039	0.224	0.173
	0.40 – 0.50	+0.013	0.074	0.244	0.061	0.270	0.287
	0.50 – 0.60	+0.016	0.081	0.258	0.073	0.246	0.290
	0.60 – 0.70	–0.001	0.047	0.137	0.044	0.218	0.177
	0.70 – 0.80	–0.010	0.053	0.088	0.054	0.138	0.152
	0.80 – 0.90	–0.012	0.053	0.095	0.050	0.161	0.151
	0.90 – 1.00	–0.002	0.055	0.144	0.055	0.192	0.184
	1.00 – 1.10	–0.028	0.088	0.239	0.111	0.091	0.259
	1.10 – 1.20	–0.019	0.064	0.146	0.076	0.134	0.195
Mizuki	1.20 – 1.30	–0.003	0.061	0.101	0.062	0.137	0.162
	1.30 – 1.40	–0.003	0.064	0.156	0.067	0.179	0.204
	1.40 – 1.50	–0.006	0.064	0.228	0.069	0.244	0.242
	1.50 – 1.60	+0.000	0.074	0.304	0.107	0.243	0.298
	1.60 – 1.70	+0.012	0.113	0.329	0.153	0.101	0.332
	1.70 – 1.80	+0.043	0.161	0.369	0.175	0.077	0.394
	1.80 – 1.90	+0.033	0.169	0.385	0.172	0.080	0.398
	1.90 – 2.00	+0.017	0.160	0.361	0.160	0.117	0.383
	2.00 – 2.10	+0.019	0.161	0.341	0.149	0.102	0.376
	2.10 – 2.20	+0.009	0.148	0.297	0.139	0.108	0.361
	2.20 – 2.30	+0.024	0.166	0.347	0.153	0.128	0.404
	2.30 – 2.40	+0.028	0.166	0.369	0.161	0.157	0.420
	2.40 – 2.50	+0.011	0.146	0.362	0.148	0.199	0.405
	2.50 – 2.60	+0.029	0.143	0.389	0.150	0.213	0.413
	2.60 – 2.70	+0.019	0.142	0.385	0.132	0.285	0.426
	2.70 – 2.80	+0.000	0.141	0.390	0.101	0.355	0.433
	2.80 – 2.90	–0.004	0.165	0.445	0.081	0.439	0.491
	2.90 – 3.00	+0.006	0.181	0.483	0.076	0.479	0.508
	3.00 – 3.10	+0.006	0.130	0.435	0.062	0.444	0.476
	3.10 – 3.20	+0.790	0.834	0.532	1.229	0.000	0.566
	3.20 – 3.30	+0.082	0.275	0.504	1.196	0.083	0.551
	3.30 – 3.40	+0.116	0.327	0.518	1.787	0.000	0.558
	3.40 – 3.50	+0.006	0.151	0.465	0.050	0.503	0.504
	3.50 – 3.60	+0.005	0.079	0.337	0.047	0.381	0.382
	3.60 – 3.70	+0.006	0.077	0.345	0.048	0.375	0.390
	3.70 – 3.80	+0.006	0.119	0.444	0.055	0.464	0.485
	3.80 – 3.90	+0.026	0.103	0.316	0.061	0.321	0.380
	3.90 – 4.00	–0.003	0.160	0.491	0.054	0.505	0.525
	0.00 – 0.10	–99.000	–99.000	–99.000	–99.000	–99.000	–99.000
	0.10 – 0.20	+0.016	0.068	0.170	0.054	0.207	0.234
	0.20 – 0.30	+0.013	0.072	0.256	0.055	0.297	0.287
	0.30 – 0.40	+0.002	0.053	0.182	0.050	0.251	0.226
	0.40 – 0.50	+0.011	0.070	0.194	0.064	0.210	0.241
	0.50 – 0.60	–0.001	0.065	0.217	0.054	0.258	0.249
	0.60 – 0.70	+0.000	0.038	0.117	0.035	0.207	0.148
	0.70 – 0.80	–0.005	0.050	0.132	0.054	0.184	0.171
	0.80 – 0.90	–0.009	0.053	0.089	0.054	0.142	0.148
	0.90 – 1.00	–0.001	0.048	0.148	0.046	0.221	0.174
	1.00 – 1.10	–0.019	0.075	0.205	0.095	0.135	0.229
	1.10 – 1.20	–0.011	0.054	0.124	0.056	0.164	0.167
MLZ	1.20 – 1.30	–0.010	0.060	0.093	0.058	0.128	0.152
	1.30 – 1.40	–0.009	0.063	0.140	0.068	0.159	0.189
	1.40 – 1.50	–0.000	0.082	0.319	0.128	0.177	0.305
	1.50 – 1.60	–0.018	0.072	0.291	0.106	0.215	0.285
	1.60 – 1.70	–0.032	0.115	0.335	0.152	0.087	0.338
	1.70 – 1.80	+0.006	0.134	0.320	0.159	0.076	0.355
	1.80 – 1.90	+0.024	0.143	0.315	0.151	0.106	0.357
	1.90 – 2.00	+0.032	0.152	0.319	0.145	0.102	0.362
	2.00 – 2.10	+0.013	0.139	0.275	0.129	0.097	0.334
	2.10 – 2.20	+0.023	0.137	0.285	0.133	0.081	0.338
	2.20 – 2.30	+0.034	0.155	0.316	0.144	0.090	0.371
	2.30 – 2.40	+0.044	0.168	0.369	0.149	0.102	0.403
	2.40 – 2.50	+0.073	0.174	0.433	0.165	0.131	0.430
	2.50 – 2.60	+0.059	0.154	0.391	0.160	0.167	0.418
	2.60 – 2.70	+0.031	0.134	0.371	0.145	0.226	0.402
	2.70 – 2.80	+0.030	0.157	0.419	0.149	0.298	0.445
	2.80 – 2.90	+0.019	0.155	0.429	0.110	0.368	0.456
	2.90 – 3.00	+0.004	0.150	0.441	0.080	0.431	0.472
	3.00 – 3.10	–0.013	0.144	0.450	0.064	0.460	0.494
	3.10 – 3.20	–0.013	0.171	0.479	0.066	0.487	0.526
	3.20 – 3.30	–0.003	0.145	0.449	0.061	0.465	0.488
	3.30 – 3.40	–0.011	0.115	0.407	0.057	0.440	0.454
	3.40 – 3.50	–0.008	0.092	0.355	0.048	0.389	0.400
	3.50 – 3.60	–0.002	0.077	0.318	0.050	0.344	0.368
	3.60 – 3.70	–0.001	0.080	0.326	0.048	0.360	0.371
	3.70 – 3.80	–0.007	0.081	0.266	0.051	0.282	0.327
	3.80 – 3.90	+0.015	0.101	0.293	0.064	0.309	0.355
	3.90 – 4.00	–0.000	0.076	0.290	0.050	0.303	0.343
	0.00 – 0.10	+0.009	0.042	0.067	0.037	0.113	0.109
	0.10 – 0.20	–0.001	0.054	0.147	0.047	0.197	0.196

Table 3. (Continued)

	0.20 – 0.30	–0.000	0.061	0.207	0.060	0.252	0.242
	0.30 – 0.40	–0.004	0.045	0.153	0.043	0.243	0.198
	0.40 – 0.50	–0.002	0.061	0.199	0.053	0.245	0.237
	0.50 – 0.60	+0.001	0.067	0.230	0.054	0.268	0.262
	0.60 – 0.70	+0.001	0.042	0.169	0.036	0.257	0.196
	0.70 – 0.80	+0.000	0.047	0.165	0.045	0.243	0.195
	0.80 – 0.90	–0.010	0.052	0.123	0.054	0.180	0.170
	0.90 – 1.00	–0.004	0.047	0.192	0.041	0.271	0.198
	1.00 – 1.10	–0.021	0.069	0.222	0.097	0.137	0.230
	1.10 – 1.20	–0.012	0.051	0.139	0.051	0.192	0.170
NNPZ	1.20 – 1.30	–0.004	0.050	0.092	0.050	0.146	0.141
	1.30 – 1.40	–0.002	0.055	0.121	0.057	0.164	0.164
	1.40 – 1.50	–0.004	0.057	0.198	0.059	0.243	0.216
	1.50 – 1.60	–0.005	0.067	0.268	0.069	0.277	0.269
	1.60 – 1.70	–0.018	0.107	0.302	0.142	0.124	0.317
	1.70 – 1.80	–0.001	0.132	0.333	0.158	0.089	0.353
	1.80 – 1.90	+0.008	0.137	0.311	0.145	0.125	0.350
	1.90 – 2.00	+0.009	0.131	0.267	0.124	0.096	0.322
	2.00 – 2.10	+0.013	0.124	0.251	0.118	0.110	0.312
	2.10 – 2.20	+0.026	0.140	0.295	0.132	0.108	0.353
	2.20 – 2.30	+0.016	0.146	0.321	0.138	0.130	0.362
	2.30 – 2.40	+0.022	0.138	0.299	0.136	0.138	0.355
	2.40 – 2.50	+0.036	0.141	0.382	0.149	0.163	0.393
	2.50 – 2.60	+0.026	0.136	0.348	0.134	0.214	0.389
	2.60 – 2.70	+0.019	0.119	0.347	0.118	0.254	0.389
	2.70 – 2.80	–0.002	0.106	0.310	0.081	0.300	0.357
	2.80 – 2.90	+0.001	0.104	0.277	0.077	0.272	0.348
	2.90 – 3.00	+0.006	0.088	0.291	0.071	0.293	0.344
	3.00 – 3.10	+0.003	0.101	0.327	0.066	0.336	0.381
	3.10 – 3.20	–0.004	0.100	0.317	0.068	0.341	0.378
	3.20 – 3.30	–0.006	0.086	0.326	0.055	0.355	0.377
	3.30 – 3.40	–0.009	0.102	0.375	0.055	0.412	0.422
	3.40 – 3.50	–0.005	0.068	0.322	0.041	0.380	0.365
	3.50 – 3.60	+0.003	0.073	0.301	0.048	0.339	0.349
	3.60 – 3.70	+0.007	0.070	0.253	0.050	0.289	0.309
	3.70 – 3.80	+0.011	0.081	0.259	0.055	0.274	0.318
	3.80 – 3.90	+0.013	0.070	0.230	0.050	0.246	0.289
	3.90 – 4.00	+0.001	0.088	0.277	0.061	0.298	0.345

key	description
object_id	unique object id to be used to join with the photometry tables
photoz_X	Photo- <i>z</i> point estimate where X is either mean, mode, median, or best.
photoz_mc	Monte Carlo draw from the full PDF
photoz_conf_X	Photo- <i>z</i> confidence value defined by equation 15 at photoz_X.
photoz_risk_X	Risk parameter defined by equation 13 at photoz_X.
photoz_std_X	Second order moment around a point estimate (photoz_X) derived from full PDF.
photoz_err68_min	16 % percentile in the PDF
photoz_err68_max	84 % percentile in the PDF
photoz_err95_min	2.5 % percentile in the PDF
photoz_err95_max	97.5 % percentile in the PDF

Table 4. Common photo-*z* parameters available for all the codes.

CODE	target selection	number of objects	other quantities
DEmP	<code>detect_is_primary</code> is True	171,721,095	None
EPHOR	objects with CModel fluxes in all five bands	197,227,501	None
EPHOR_AB	objects with afterburner fluxes in all five bands	221,617,662	None
FRANKEN-Z	<code>detect_is_primary</code> is True objects with afterburner fluxes in all five bands	135,966,862	many
Mizuki	<code>detect_is_primary</code> is True objects with CModel fluxes in at least three bands	144,107,354	many
MLZ	<code>detect_is_primary</code> is True	171,721,095	flux flag
NNPZ	<code>detect_is_primary</code> is True objects with CModel fluxes in all five bands	163,627,623	neighbor redshifts and weights

Table 5. Target selection applied by each code. The number of objects that satisfy the selection is shown. Details of other quantities available in the catalog can be found in Section 7.